

The Temporal Behavior of Numerically Simulated Multicell-Type Storms. Part II: The Convective Cell Life Cycle and Cell Regeneration

ROBERT G. FOVELL AND PEI-HUA TAN

Department of Atmospheric Sciences, University of California, Los Angeles, Los Angeles, California

(Manuscript received 14 November 1996, in final form 14 July 1997)

ABSTRACT

The authors study herein the convective cell life cycle and the cell generation process in mature, multicellular squall-line storms possessing well-developed subcloud cold pools using two- and three-dimensional models. The multicellular storm establishes new cells on its forward side, in the vicinity of the forced updraft formed at the pool boundary, that first intensify and then decay as they travel rearward within the storm's upward sloping front-to-rear airflow. The principal effort is expended on the two-dimensional case owing to the strong similarity in basic behavior seen in the two geometries.

The cell life cycle is examined in several complementary fashions. The cells are shown to be convectively active entities that induce local circulations that alternately enhance and suppress the forced updraft, modulating the influx of the potentially warm inflow. This transient circulation also drives the episodic mixing of stable air into the inflow that results in the cell's ultimate dissipation. The timing of cell regeneration is also examined; an explanation involving two separate and successive phases, each with their own timescales, is proposed. The second of these phases can be shortened if a "convective trigger," another by-product of the cell's circulation, is present in the storm's inflow environment. Sensitivity of the results to strictly numerical model details is also discussed.

1. Introduction

The mature squall line often appears as a narrow, quasi-linear band of intense convection trailed by a wider zone of light precipitation. Prominent in its circulation is an ascending "front-to-rear" (FTR) jet (Houze 1993, 348), largely consisting of air drawn from the low-level environmental inflow, that resides above a subcloud cold-air pool maintained by the evaporation of hydrometeors falling from the jet. The cold pool spreads along the surface, and convergence at its leading edge, or *gust front*, creates the forced updraft that provides the initial lift required by the potentially warm inflowing air parcels to reach their level of free convection (LFC).

The overall quasi-steady dynamics of the squall-line storm are now fairly well understood [see survey by Houze (1993)]. The FTR airflow itself, however, is rarely steady. Instead, convective "cells," short-lived discrete elements representing locally concentrated convective activity, are often found embedded within. New cells typically form on the storm's forward side, in or near the forced updraft, and subsequently travel rearward within the FTR jet, ultimately to be replaced by another cell. The cell life cycle, comprising initiation,

maturation, and decay, typically spans an hour or less (Browning et al. 1976). A cross section normal to the squall line reveals a "multicellular" family of cells, each representing a different stage in the life cycle. As the longevity of the multicellular storm seems largely due to its ability to generate new, replacement cells, the cell life cycle and generation mechanisms involved in new cell establishment are important topics for study.

The cell life cycle has been shown to be sensitive to a wide variety of factors, including (but not limited to) the amount and distribution of vertical wind shear (Thorpe et al. 1982; Dudhia et al. 1987; Fovell and Ogura 1989; and Fovell and Dailey 1995) and model microphysics (Fovell and Ogura 1988). It has often been noted that new cells tend to form in or near the gust front's forced updraft, but not until previously established cells have moved rearward within the FTR airflow. This has sometimes been interpreted as a horizontal advective timescale (Miller 1978; Thorpe et al. 1982; Wilhelmson and Chen 1982; Fovell and Ogura 1989), though this raises the questions of how and why cells become discrete (or "cut off") from the forced lifting as well as how and when new cells will form. Hane et al. (1987), for example, hypothesized that periodic convergence enhancement at the gust front, caused by the spreading of the previous cell's downdraft along the surface, could represent one controlling factor influencing the timing of new cell generation. Wilhelmson and Chen (1982), on the other hand, discounted this relationship.

Corresponding author address: Robert G. Fovell, Dept. of Atmospheric Sciences, University of California, Los Angeles, Los Angeles, CA 90095-1565.
E-mail: fovell@atmos.ucla.edu

Recently, Yang and Houze (1995, hereafter YH) interpreted the convective cells as being manifestations of vertically trapped, rearward propagating gravity waves. In their view, the cutoff process is a transient gravity wave response to the forced updraft's nearly steady forcing, and rearward cell propagation can be described in terms of gravity wave phase speeds. This interpretation was based on their observation that convective cell updrafts come to acquire the typical signatures of rearward propagating gravity waves, which include a "quadrature" phase relationship between local warming (positive potential temperature perturbation) and upward motion, with the former leading (i.e., rearward of) the latter by one-quarter wavelength in the direction of the wave's motion.

This study examines the convective cell life cycle and the cutoff process, including factors influencing subsequent new cell generation. In the simulations presented herein, the convective cells *themselves* do not behave as gravity waves until they (or remnants thereof) have become convectively inactive. That occurs late in the life cycle when the cells have passed into the storm's trailing region, far from the leading edge of the storm. By that time, new cell development has usually already occurred at the storm's leading edge. Instead, the cutoff process will be shown to result from the cell's own induced local circulation that also causes the episodic mixing of stable air into its inflow. This mixing erodes the cell's convective instability, and thus the cell effectively sows the seeds of its own demise. As they mature, the cells do eventually manifest quadrature phasing between local warming and upward motion, but this is due to the detrainment of the cell's original, least diluted, and thus most positively buoyant air. The cell's own induced circulation not only undermines the cell itself, but also appears to help hasten the next convective development.

The structure of this paper is as follows. In section 2, the model setup and initial conditions are described. Section 3 presents the two- and three-dimensional simulations that are examined in more detail in section 4. That section presents an analysis of the cell life cycle, including cell generation mechanisms, based on the equations of motion and potential temperature and also passive tracers. Finally, in section 5, we present a synthesized description of the convective cell life cycle and discuss the differences between YH's conclusions and our own. The sensitivity of these results to strictly numerical details is discussed in the appendix.

2. Model description and initialization

This study employed the fully compressible ARPS¹ model in its two- and three-dimensional configurations. The thermodynamic sounding [see Fig. 2 of Fovell and

Ogura (1988)] used for the horizontally homogeneous base state was adapted from the 22 May 1976 Oklahoma squall-line event (Ogura and Liou 1980; Smull and Houze 1985). This favorable sounding possesses about 2500 J kg⁻¹ of convective available potential energy (CAPE) and virtually no convective inhibition for a parcel rising undiluted from the 1.3-m-deep mixed layer. The lifting condensation and free convection levels coincide at about 1.6 km, and the equilibrium level is approximately 10.6 km, again for an undiluted parcel. This sounding was also used in Fovell and Ogura (1989), Fovell (1991), and Fovell and Dailey (1995, hereafter FD), all of which employed a 2D anelastic model.

The 2D simulation employed FD's $D = 2.5$ wind profile, possessing 7.5 m s⁻¹ of speed change over the lowest 2.5 km and zero shear above. The 3D run used their $D = 5$ profile, with 15 m s⁻¹ of speed change over 5 km (and thus the same shear over the lowest 2.5 km) without directional shear. As in FD, convection was initiated with a horizontally symmetric warm bubble (maximum potential temperature excess 2 K). These simulations employed the available second-order centered advection, Smagorinsky–Lilly subgrid turbulence and Kessler (1969) microphysical schemes, and neglected surface friction and fluxes, Coriolis terms, radiative effects, and the ice phase. The domain was 22 km deep between flat plates and vertical grid stretching enhanced resolution (minimum grid spacing 200 m) near the surface. A weak absorbing layer was placed in the model stratosphere.

Both model geometries used constant, 1-km horizontal resolution. The 2D domain width was 600 km while the 3D domain's horizontal area was 100 km × 100 km. Storms typically develop much faster in the 3D geometry, and this is fortuitous because practical considerations limited the 3D domain size. The lateral boundaries were open, except at the 3D run's northern edge, where a mirror condition exploiting the unidirectional shear and symmetric initial perturbation was used. This made the actual computational domain 50 km wide in the y direction. Galilean transformations kept the convection away from the lateral boundaries. The 2D and 3D simulations were run for 8 and 3 h, respectively.

The ARPS model uses the Klemp–Wilhelmson (1978) "time splitting" scheme that integrates acoustically active and inactive terms on separate time steps, taken to be 1 and 6 s, respectively. The acoustic wave speed was a vertically varying function of the base state, and was not artificially reduced. Computational smoothing was applied to perturbations from the base state for all variables (excluding pressure) to control numerical instability. The second-order scheme was used in the vertical direction; in the horizontal, fourth-order smoothing was chosen for its relatively greater scale selectivity. The dissipation rates for both were 10⁻³ s⁻¹.

Although only two simulations are shown, the basic results described herein have been verified in a large number of simulations conducted with the (2D) anelastic and (2D and 3D) ARPS models in which many physical

¹ Advanced Regional Prediction System, documented in Xue et al. (1995).

and numerical factors relating to the initial environment and model setup were varied. Different shear intensities and distributions, microphysical and turbulence parameterizations and settings, horizontal and vertical resolutions, domain widths and depths, boundary conditions, advection schemes, Galilean (domain) translation speeds, and computational dissipation rates were examined. While some factors influenced specific details relating to the storms' temporal behaviors and spatial structures, the storms were all dynamically similar regarding their multicellular unsteadiness, longevity, and convective cell life cycle characteristics. For example, we found that the vertical computational smoothing had relatively little impact on the results but the horizontal smoothing did influence the storms' convective-scale structures and sensitivity to the Galilean translation (see appendix). Even so, a fundamental dynamical similarity was still strongly evident.

3. Description of the 2D and 3D simulations

a. The 2D simulation

The 2D model storm reached maturity before 5 h. In virtually all respects, the storm was strongly qualitatively similar to FD's (anelastic) version of this case. As FD described that case in detail, we focus solely upon aspects relevant to the cell life cycle.

During its mature phase, the storm's ground relative motion was eastward at 15.3 m s^{-1} and it generated new cells at approximately 11-min intervals in a simply periodic fashion. This period will be referred to as the "cell generation cycle" or "repeat cycle." Most of the storm's principal tropospheric features moved toward the storm's rear with time. These will be discussed in the *storm's reference frame*. Thus, the west side of an updraft will be denoted its "rearward" or "rear-facing" side, though it is its forward side with respect to its own motion.

Figure 1 shows vertical velocity w and perturbation potential temperature² θ' fields at four times (labeled A–D) sampling one of the mature phase cell generation cycles. At time A (Fig. 1a), a still intensifying updraft (cell n) was located in the middle troposphere (above $x = 32$), rearward of the gust from forced updraft (at $x = 39$). The remnants of a still older development (cell $n - 1$) resided farther rearward (above $x = 16$). Three minutes later (Fig. 1b), at time B, cell n had reached its maximum strength, and the now isolated forced updraft was intensifying and expanding vertically. Mature cell n was entering its dissipating stage and rapidly weakened and disorganized during the next three minutes (leading to time C; Fig. 1c). At this time, several "updraft centers" were found between $22 \leq x \leq 32$; the dissociation continued through time D (Fig. 1d) and beyond.

² All perturbation fields were computed relative to the horizontally homogeneous base state.

In the meantime, a new cell ($n + 1$) became identifiable above the forced updraft by time C (Fig. 1c). As the repeat cycle neared its conclusion (time D; Fig. 1d), the rearward-propagating new cell intensified rapidly. Two minutes later, owing to its periodicity, the storm state was nearly the same as that seen at time A (Fig. 1a), with original cell $n + 1$ having become cell n while the original cell n had disintegrated into cell $n - 1$. The ensuing discussion exploits this periodicity.

We note below three specific aspects relating to cell generation in general and in the storm's unsteadiness in particular. First, following initiation, the new cell was "cut off" from the forced lifting and became an independent, rearward-propagating updraft. This cutoff process appears to be an integral part of the multicell storm's unsteadiness. Second, as shown in Fig. 2, the forced updraft strength was persistent yet unsteady, fluctuating by several meters per second during the cell cycle. At each time step, the strongest ascent in the forced updraft at the $z \sim 1.4 \text{ km}$ level was identified and then averaged with the vertical velocities recorded at the eight surrounding grid points. The forced updraft was weakest just prior to the new cell's appearance (time A), intensified as the new cell became established (until time C), and finally declined as the cell started its rearward movement (times C through A). This variation may be important in explaining how the developing cell became cut off and why the storm itself was unsteady.

Third, as a cell updraft aged, the location of the largest positive θ' anomaly within it shifted. In the new cell $n + 1$ at time C, the anomaly and strongest ascent were collocated. The warming resulted from vapor condensation, the rate of which was largest where the ascent was strongest. As the cell aged and intensified (times D and A), the warmest air became concentrated along the updraft's top- and rear-facing sides (see above $x = 31$ in Fig. 1a). By time C, the anomaly weakened and came to be located well to the rear of the strongest updraft center (see above $x = 27$ in Fig. 1c) in the rapidly disorganizing cell, which brought the anomaly and updraft into quadrature. As the cell's remnants propagated farther rearward, this phasing usually persisted. Yang and Houze (1995) based their analysis on the presence of this quadrature phasing.

Equivalent potential temperature θ_e , nearly conserved apart from mixing and precipitation fallout,³ provides a somewhat different view of the cutoff process and the storm's unsteadiness (Fig. 3). As the forced updraft intensified after time A (Fig. 3a), high- θ_e air began rising upward from the storm's low-level inflow. This created

³ The θ_e was computed using (4.5.11) from Emanuel (1994) which explicitly includes water loading in the calculation. Reduction of water loading, by means of precipitation fallout, can locally increase θ_e . This effect can be seen in the figure [in and above the center of the mature updraft in panels (a) and (d), above $x = 32$ and 34 km , respectively].

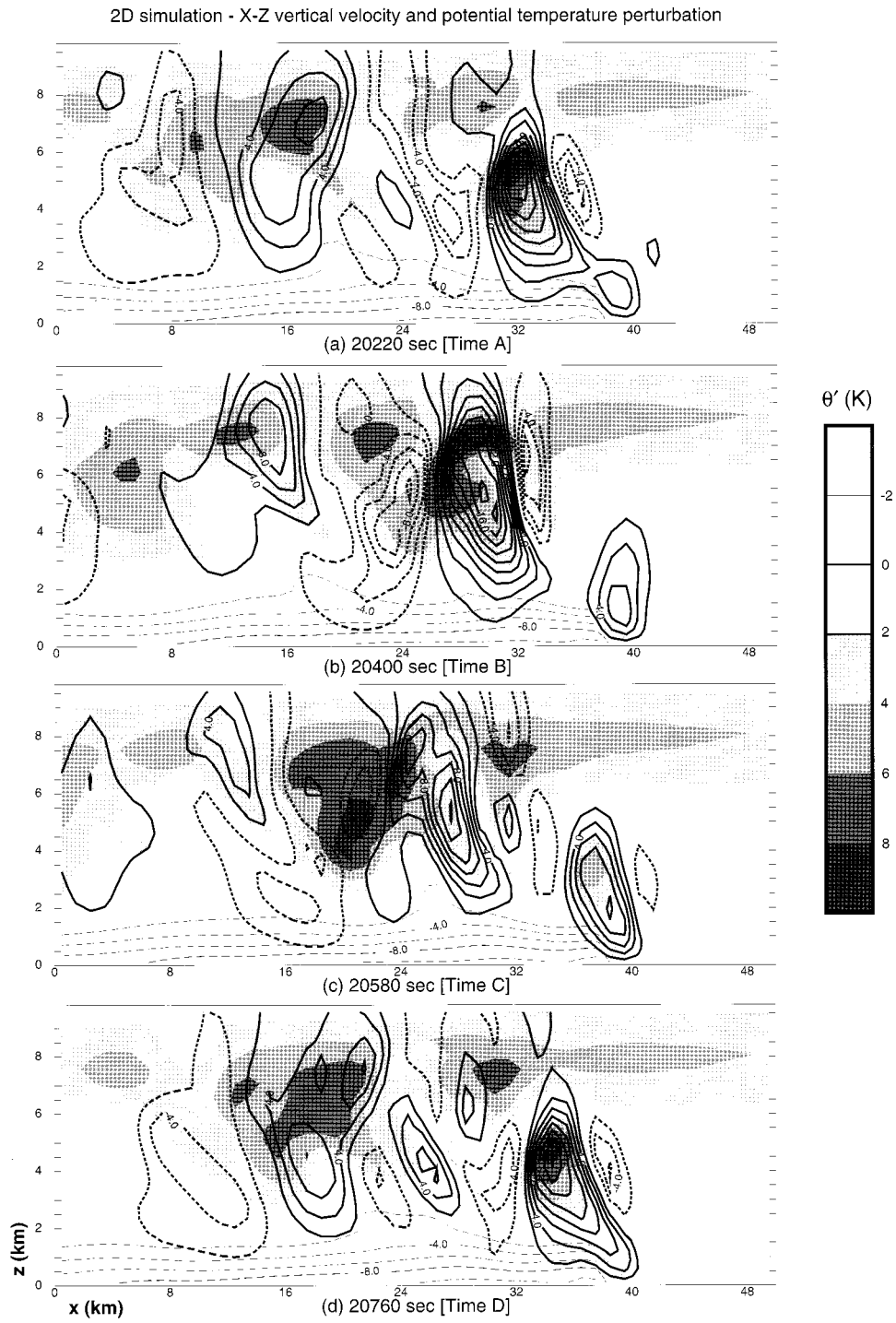


FIG. 1. Vertical velocity w (2 m s^{-1} contours) and potential temperature perturbation θ' (shaded) fields for a $50 \text{ km} \times 10 \text{ km}$ subdomain at four times (labeled A–D) during one cell generation cycle for the 2D simulation. Abscissa coordinates are subdomain relative. Negative contours are dashed and the zero contour is omitted. For θ' , contours (interval 2 K) are included for negative values less than or equal to -2 K only.

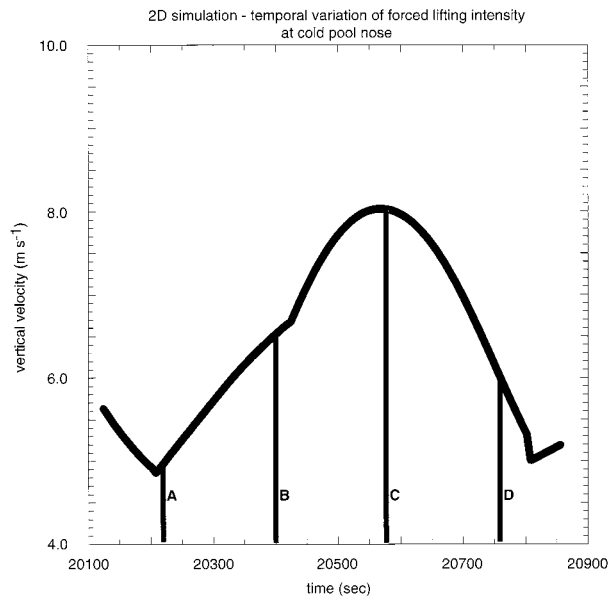


FIG. 2. Time series illustrating the forced updraft's temporal variation for the 2D simulation spanning a period incorporating the four times (labeled A–D) depicted in Fig. 1.

a “ribbon” of high- θ_e air that subsequently extended farther upward and rearward (above $x = 39$ in Figs. 1b and 1c), carried by the new development. However, a portion of the ribbon began to erode through mixing almost immediately. By time D (Fig. 3d), a patch of the highest- θ_e air had become isolated at the top of the weakened ribbon; note the decrease in θ_e that occurred above $x = 37$ appeared as the forced updraft's strength declined (Fig. 2). As this updraft's intensity controls the rate of high- θ_e inflow into the storm, its temporal variation appears relevant to the storm's unsteadiness. This variation alone cannot fully explain the ribbon's dilution, however, as mixing of lower- θ_e air into the ribbon had to have occurred.

Once cut off, the isolated high- θ_e air patch, representing the *cell's original and least diluted air*, continued rising both with and within the cell updraft. By time A (Fig. 3a), it had become concentrated at the top of the intensifying cell, not unlike the situation depicted in Blyth et al.'s (1988) conceptual model (their Fig. 14). This air subsequently *detrained* from the updraft as weakening commenced (see box in Figs. 3b and 3c). By time C (Fig. 3c), a portion of this original air had reached the principal updraft's rear-facing side. Figures 1 and 3 reveal a direct relationship between the positive θ' anomaly and the original high- θ_e air existed, at least into the cell's dissipating stage. By itself, a positive θ' anomaly does not reveal whether subsaturated descent (adiabatic compression warming) or saturated ascent (diabatic heating) created it. The collocation of the θ' and θ_e maxima, however, suggests a diabatic cause, despite the eventual development of gravity wave-like

quadrature phasing. The original air's identity was lost soon thereafter.

The θ_e fields demonstrate that the cell's principal updraft was dynamically active and moved rearward *more slowly* than its original air (see section 4a, below). From its initiation through maturity, the cell updraft resided atop the slanting high- θ_e ribbon that emanated from the low-level inflow. In saturated air, a vertical decrease of θ_e indicates convective instability, where (in the absence of mixing) rising motion generates net warming as latent heating exceeds adiabatic cooling. The updraft remained strong while being fed by this original, least diluted air. As that original air detrained, however, the updraft received parcels that were drawn into the FTR airflow after the cell was initiated, and these parcels had been subjected to mixing. Figure 3 shows the mature cell ($x \sim 30$ in Figs. 3b and 3c) weakened rapidly as the ribbon's vertical θ_e gradient decreased. The rearward movement of the progressively eroding ribbon can be seen by cycling through Fig. 3's panels.

The interruption of vapor inflow by new cell development upstream has been frequently suggested as a cause of an older cell's dissipation. On the basis of the θ_e fields, we hypothesize that a cell's ultimate dissipation is assured very early in its own life cycle, long before another cell appears and even before the cell itself has matured, when the high- θ_e (and vapor) inflow is temporarily reduced by the weakening forced updraft. In section 4b, the forced updraft's temporal variation will be shown to be a response to the cell's induced circulation. Then, mixing inexorably dilutes the high- θ_e ribbon, dampening the instability available to the cell. In section 4c, the cell's own circulation is shown to assist in this dilution, which would occur even if subsequent development did not appear upstream. Thus, we believe *cell dissipation is brought on by processes occurring within it*.

b. The 3D simulation

Attention is now turned to the 3D simulation, carried out to assess whether the most important dynamics involved in convective cell establishment can be captured in the more easily analyzed 2D geometry. One phenomenon the 2D model cannot represent is tilting of horizontal vorticity associated with the vertical wind shear to create vertical vorticity. As summarized by Klemp (1987), an updraft can lift vortex tubes aligned perpendicular to the vertical shear vector, thereby establishing counterrotating horizontal vortices (i.e., vertical vorticity) on its flanks. If the rotation is sufficiently strong, it can induce a dynamical “splitting” of the updraft that can then lead to the establishment of rotating “super-cellular” updrafts under the proper conditions. Even under less “optimal” conditions, it is appropriate to gauge the effect of such splitting on the cell generation process. The direct 3D extension of the $D = 2.5$ case (not shown) resulted in a viable multicellular storm, but one in which dynamical splitting did not occur. The D

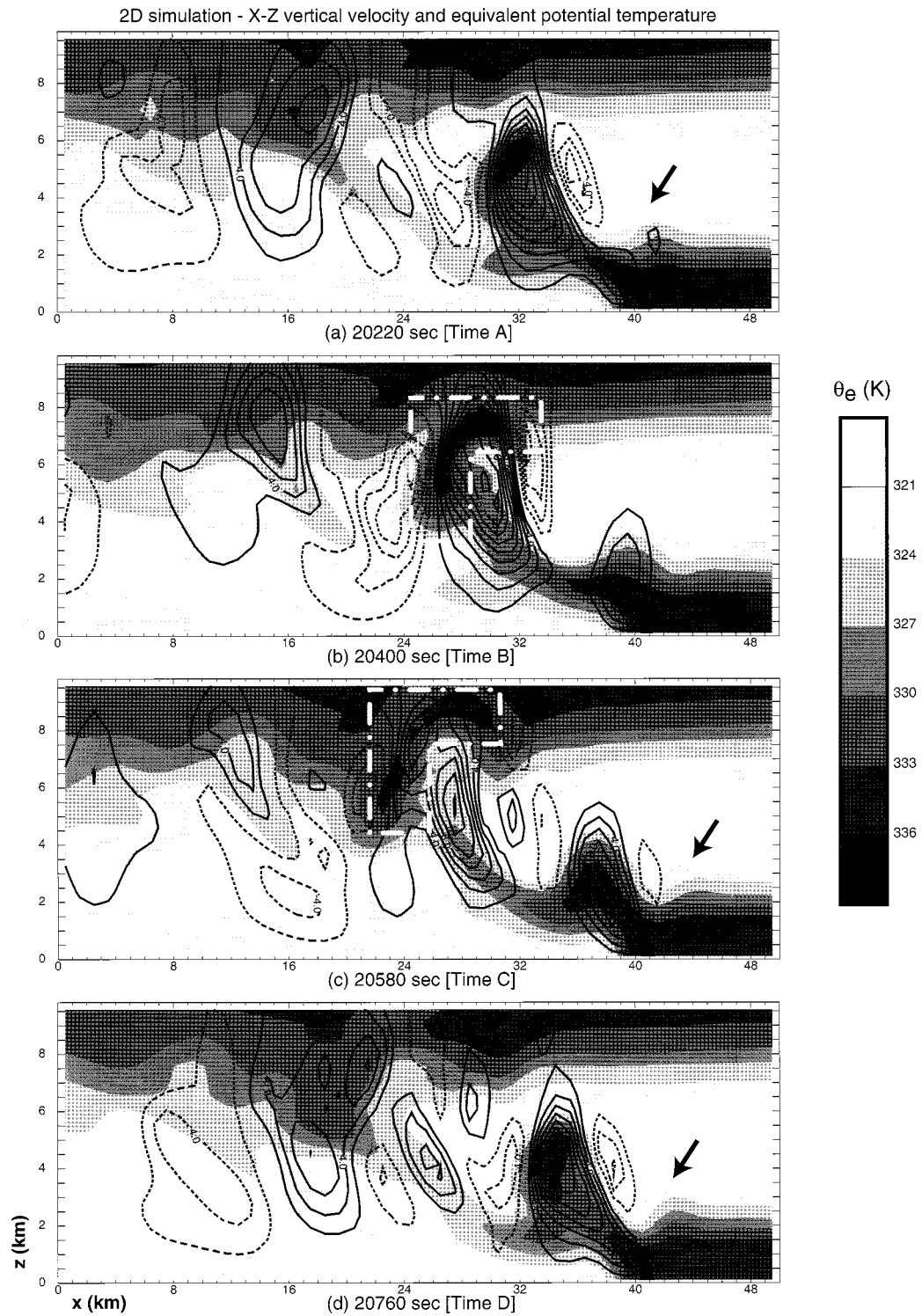


FIG. 3. As in Fig. 1 but shaded field is equivalent potential temperature θ_e . See text for discussion of areas outlined by dashed-dotted boxes and arrows highlighting the locally elevated mixed layer.

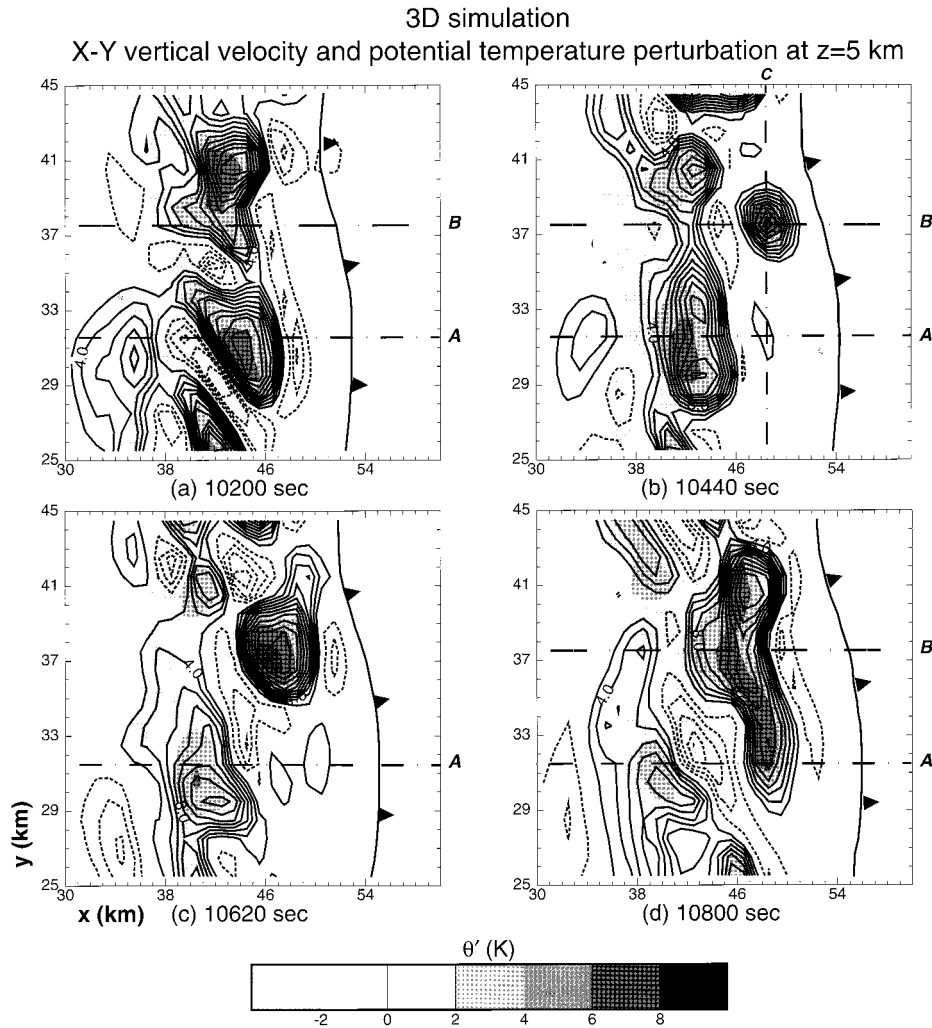


FIG. 4. Horizontal cross sections of vertical velocity (2 m s^{-1} contours) and potential temperature perturbation (shaded) taken at $z = 5$ km for four times in the 3D simulation. Flagged line indicates position of surface cold pool boundary. Only a portion of the domain is shown; axes are labeled relative to domain's southwestern corner. The symmetry axis resides at $y = 50$ km, beyond the subdomain's northern edge. The vertical cross sections of Figs. 5 and 6 are oriented along line A, and those in Fig. 12 reside along lines B and C.

= 5 simulation (see section 2) did have splitting updrafts and thus this case is presented instead.

After initiation at the northern (symmetry) boundary, the storm quickly spread in the y direction, producing a quasi-linear band of convection aligned perpendicular to the vertical shear vector by 2.5 h into the simulation. Owing to the manner of initialization, storm structure varied along the developing line, but this variation tended to diminish with time. Despite the difference in shear-layer depth between the 2D and 3D simulations, both cases developed very similar cold pools in terms of intensity and depth. Fovell and Dailey (1995) found the $D = 2.5$ and 5 cases were strongly similar with regard to these important characteristics in 2D as well.

Figure 4 shows horizontal (at $z = 5$ km) cross sections

spanning a portion of the model domain at approximately 3 h, and Fig. 5 shows vertical ($x-z$) cross sections aligned along the line labeled "A" in Fig. 4. At this time, this segment of the storm was translating eastward at about 15 m s^{-1} , comparable to the 2D storm's speed. In Fig. 4a, a mature cell updraft may be seen at $y = 31.5$, one of several arrayed along the line. Figure 5a's vertical cross section passes through the center of this cell. The updraft was neatly bisected by a vertical vorticity couplet (not shown) that undoubtedly arose from the tilting of horizontal shear vorticity. The rotation was strong enough to dynamically split the updraft shortly after the time shown. By the time of the second panel (Fig. 4b), the split members of the original mature cell had already begun moving out of the vertical plane

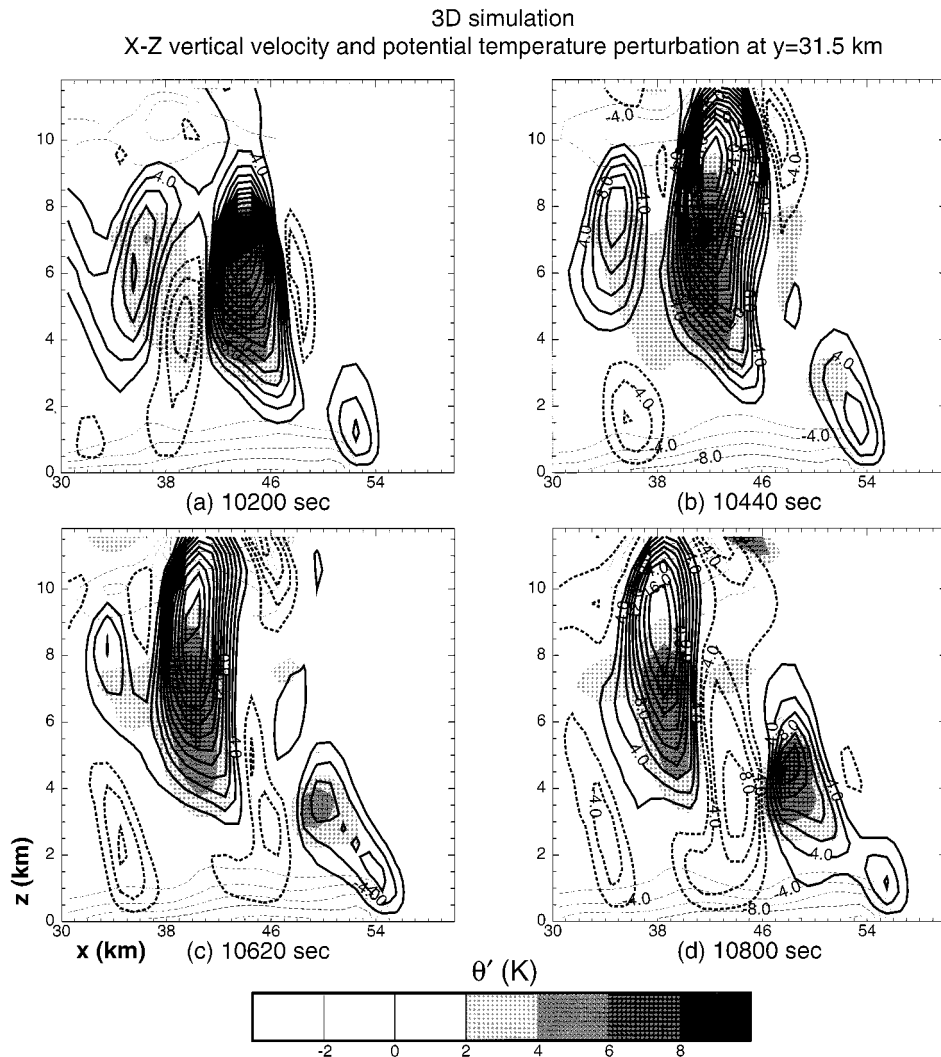


FIG. 5. Vertical cross sections of vertical velocity (contoured) and potential temperature perturbation (shaded) for the 3D simulation taken along line A ($y = 31.5$ km) shown in Fig. 4. Contour and shading intervals as in Fig. 1. Only a portion of the domain is shown, with axes indicating distance from the boundaries.

shown in Fig. 5b. Both members subsequently decayed (Figs. 4c,d), though the southern updraft's decline was significantly less rapid.

Despite the dynamical splitting, the sequence of events shown in Fig. 5 bears a strong resemblance to that seen in the 2D simulation. As the mature cell's split members moved rearward, the forced updraft again began expanding vertically, culminating in the establishment of a new cell that also subsequently propagated rearward (and split eventually as well). In this portion of the storm, the cell period was about 13 min, and its temporal behavior was roughly simply periodic [for this vertical plane, the cross section at 10 980 s (not shown) is very similar to the section at 10 200 s shown in Fig. 5a]. Thus, it appears that the splitting did not have any significant impact on the basic cell generation process,

lending credence to the belief that its basic physics can be captured in the 2D model. Also, there was insufficient shear in this case to induce supercellular behavior, which is consistent with Weisman and Klemp's (1982) results.

Although its amplitude appears smaller than in the 2D case (in this particular cross section), the forced updraft still evinced a significant temporal variation (Fig. 5). As it intensified, a high- θ_e air ribbon was established that subsequently became diluted and discontinuous (Fig. 6), just as in the 2D case (Fig. 3). As before, the updraft propagated rearward on this high- θ_e ribbon. The mature cell also moved along the line (in part due to splitting), preventing its inclusion in a single across-line cross section. The strongest portions of the mature cell shown above $x = 38$ in Figs. 5c,d resided out of the plane shown.

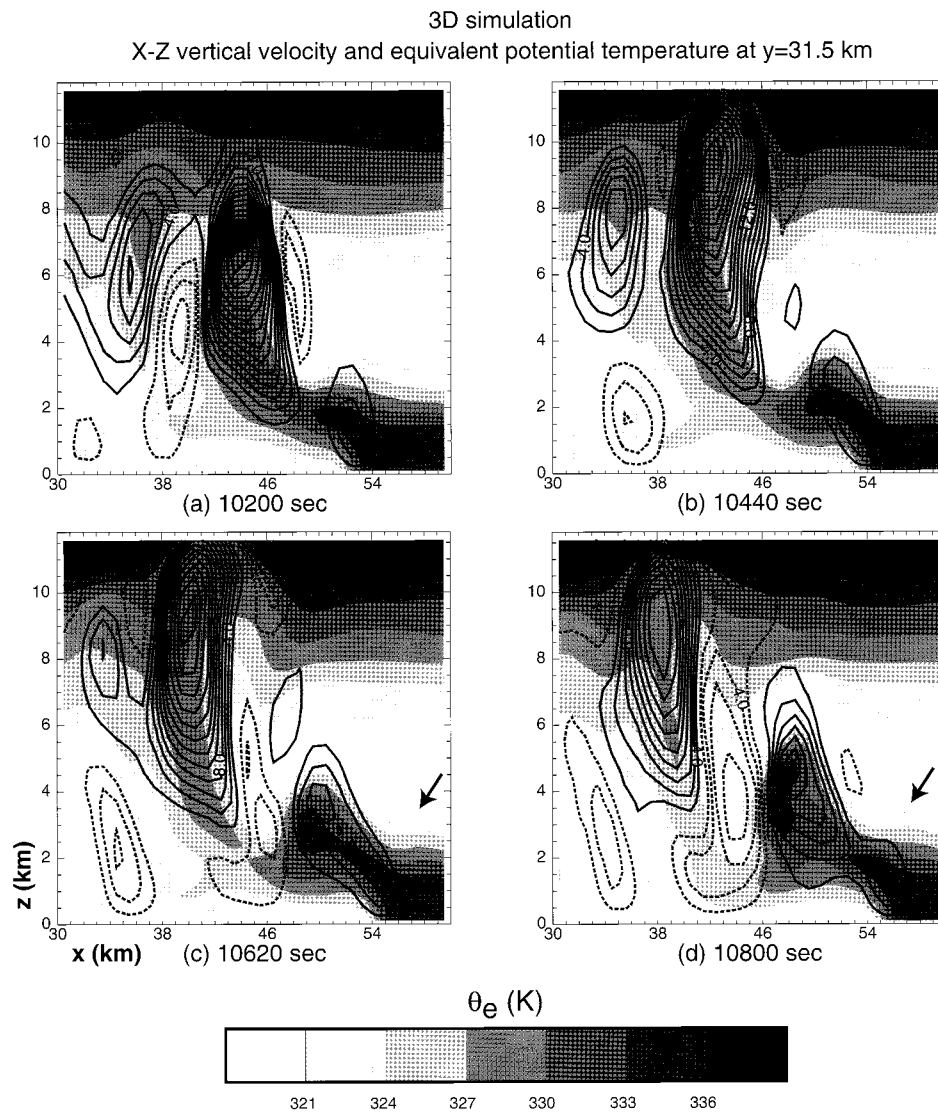


FIG. 6. As in Fig. 5 but shaded field is equivalent potential temperature. See text for discussion of arrows highlighting the locally elevated mixed layer.

4. Detailed analysis of the convective cell life cycle

In this section, we examine the cell life cycle in detail. Owing to the strong qualitative similarity between the 2D and 3D model storms, these analyses are based primarily on the 2D simulation. The examination will take place in four steps. First, in subsection (a), the roles played by various terms in the vertical velocity and potential temperature equations are discussed. In subsection (b), the forced updraft's temporal variation is explained. In subsection (c), passive tracers illuminate the cutoff process and the dilution of the high- θ_e ribbon. Finally, in subsection (d), we consider how and why the mature storm is able to establish the new cell it must generate to perpetuate itself. Each step utilizes different tools and perspectives. In section 5, we integrate these perspectives into a unified description of the cell life cycle.

a. The cell life cycle as revealed by the vertical velocity and potential temperature equations

Figure 7 shows model fields for the 2D simulation at 20 460 s, which fell between times B and C [Figs. 1b,c and 3b,c]. Five updraft features are designated. Feature 1 is the incipient new cell $n + 1$ within the forced updraft, while feature 2 is mature cell n 's updraft. At this time, the incipient cell was rapidly intensifying and the mature cell's dissipation stage had just commenced. Feature 3 is a surviving remnant of the still older development (cell $n - 1$). Updrafts 4 and 5 reside at mid-levels in the storm's trailing region. All five features were embedded in the storm's FTR airflow (Fig. 7b) and were in the process of propagating rearward.

Although the figure shows different updrafts at a single time, these features may be interpreted as representing

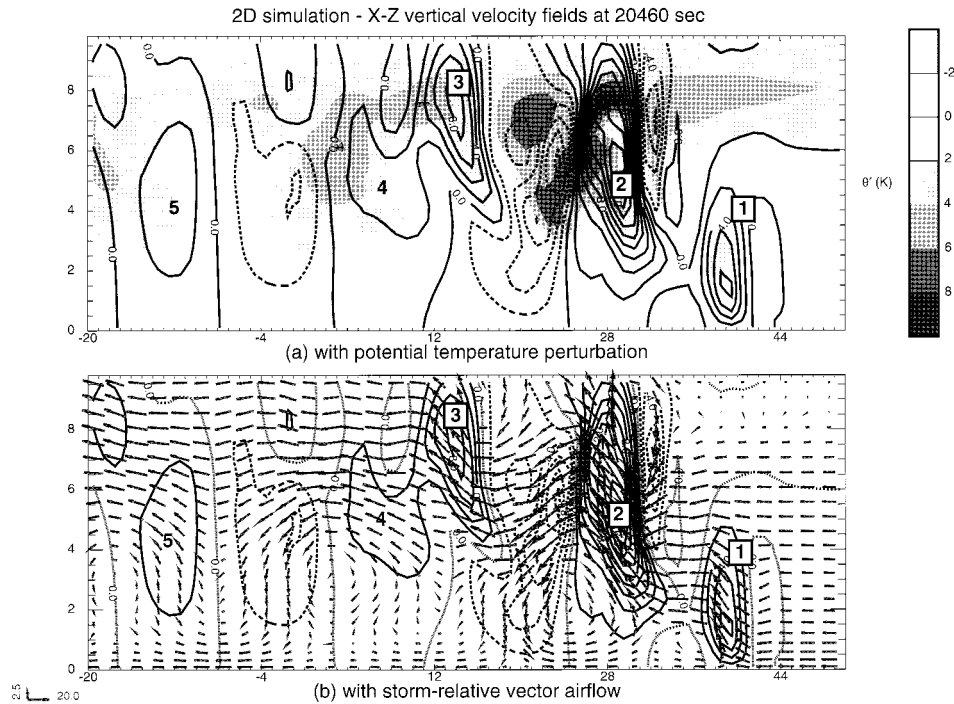


FIG. 7. Vertical velocity (2 m s^{-1} contours) field for the 2D simulation at 20460 s, which falls between Fig. 1's times B and C. Horizontal axes labeled relative to subdomain shown in Fig. 1. In (a), shaded field is potential temperature perturbation. In (b), vectors represent storm-relative airflow. The features marked 1–5 are discussed in the text.

different stages in the life cycle of a single convective cell. After the time shown (refer to Fig. 1), the incipient cell (feature 1) will first evolve into the mature cell (feature 2) and then disorganize and weaken, resulting in the decaying remnant identified as feature 3. As the cell continues disorganizing, feature 4 appears in its vicinity, which in turn evolves into updraft 5 at a still later time.

The equations governing the local (storm- or grid-relative) tendencies for vertical velocity (m s^{-2}) and perturbation potential temperature (K s^{-1}), respectively, are

$$\underbrace{\frac{\partial w}{\partial t}}_{\text{LWDT}} = \underbrace{-\mathbf{V} \cdot \nabla_{\mathbf{w}}}_{\text{WADV}} - \underbrace{\frac{1}{\bar{\rho}} \frac{\partial p'}{\partial z}}_{\text{VPGA}} + \underbrace{B'}_{\text{BUOY}} \quad (1)$$

$$\underbrace{\hspace{10em}}_{\text{PWDT}}$$

$$\frac{\partial \theta'}{\partial t} = -u \frac{\partial \theta}{\partial x} - w \frac{\partial \theta}{\partial z} + \underbrace{S(q_c)}_{\text{QCLH}} - S(q_r) \quad (2)$$

$$\underbrace{\hspace{10em}}_{\text{TVPT}}$$

Mixing terms are neglected in both equations. Variable B' is the perturbation buoyancy term (including water loading), $\bar{\rho}$ is the base-state density (a function of height alone), and the other symbols have their conventional meanings. As shown in (1), the local vertical velocity

acceleration (LWDT) may be decomposed into two parts, storm-relative vertical velocity advection (WADV) and the parcel vertical velocity acceleration (PWDT), the latter being the sum of the vertical pressure gradient (VPGA) and buoyancy (BUOY) accelerations when mixing is neglected. In section 4b, this equation will be decomposed in a different fashion.

The first two terms on the right-hand side of (2) are the horizontal and vertical advection of total potential temperature. The remaining two terms represent the diabatic effects. Variable $S(q_c)$ is the latent heating/cooling associated with cloud water condensation/evaporation (QCLH), while $S(q_r)$ is the latent cooling produced by rainwater evaporation. TVPT represents the sum of the vertical advection and diabatic terms. Local upward (downward) motion causes adiabatic expansion cooling (compression warming), which may be partially or completely offset by diabatic effects associated with water substance phase changes. Although an incomplete picture of the local potential temperature tendency, TVPT shows where vertical motion results in net warming or cooling by itself.

Figure 8 shows the instantaneous distributions of the WADV, PWDT, LWDT, and TVPT terms at 20460 s. As all five features resided in the storm's FTR airflow, advection (WADV) was carrying them rearward (Fig. 8a). Yet, none of the updrafts were passive objects. In updrafts 4 and 5, PWDT and WADV were acting in the

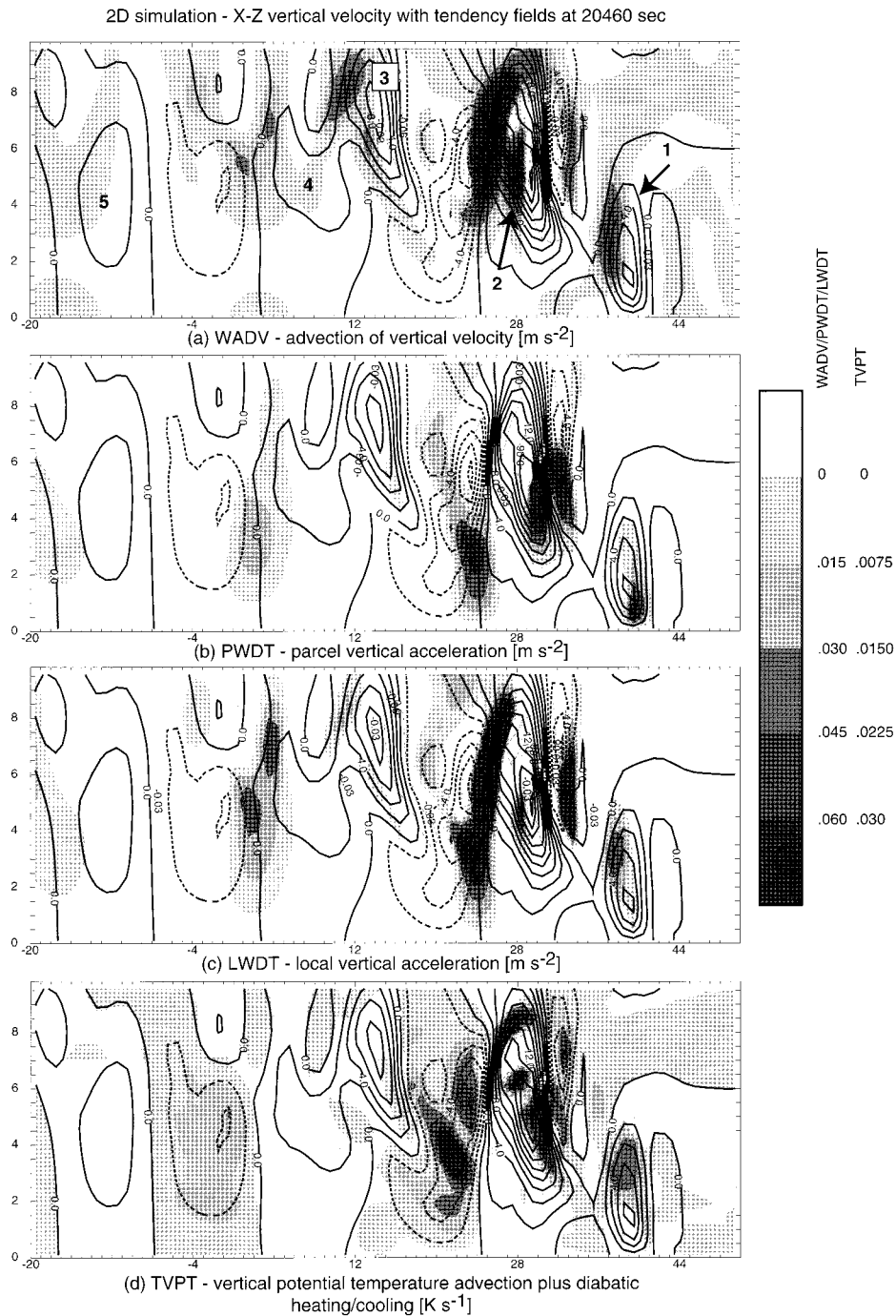


FIG. 8. As in Fig. 7 but showing tendency fields with vertical velocity ($2 m s^{-1}$ contours). Panels are (a) WADV, (b) PWDT, (c) LWDT, and (d) TVPT. For acceleration fields, upward (downward) accelerations are shaded (contoured).

same sense. Thus, these two features were moving rearward *more quickly* than the parcels embedded within them at this time (whose motions were determined by advection). In the 3 min between times B and C, updraft 4 moved from $x = 11.5$ to $x = 2.5$ km (Figs. 1b,c), for a storm-relative propagation speed of approximately 50

$m s^{-1}$, significantly faster than the speed of the embedding flow ($0-15 m s^{-1}$). Thus, the *feature*-relative airflow was eastward (i.e., toward the storm's front) in these updrafts. Note that w and θ' were in quadrature (Fig. 7a), with the warmest air leading the updrafts' motions.

The quadrature phasing is a gravity wave characteristic, but by itself is insufficient evidence that the features were indeed gravity waves. Propagation within the embedding flow is also required. Since updrafts 4 and 5 did propagate upstream relative to the parcels within them, they may be identified as being parts of a stable, rearward-propagating gravity wave. The upward motion resulted in net cooling (TVPT; Fig. 8d) as very little condensation occurred in these updrafts (not shown). These features represent the terminal phase of the cell life cycle. The convective cells degenerated into and/or caused the establishment of stable gravity waves as they moved into the trailing region, and became rapidly propagating entities in the process.

In features 2 and 3 (cells n and $n - 1$), however, the parcel acceleration and advection terms were in *opposition*, as downward (upward) parcel accelerations occurred on the rear-facing (front-facing) sides of these updrafts. This is especially obvious in feature 2, which may be more easily seen in Fig. 9a. Still, advection was dominant, and thus the local tendency LWDT (Fig. 8c) indicated net rearward motion. However, while being advected, these updrafts were actively dissipating on their rear-facing sides (in the direction of their motion) while tending to intensify on their opposite flanks. Thus, these updrafts were moving rearward more *slowly* than their embedding flows. Between times B and C (Figs. 1b,c), updraft 2's center moved from $x = 30$ to 27.5 km, a speed of about 14 m s^{-1} , which was slower than the airflow speed at the updraft's center ($\sim 30 \text{ m s}^{-1}$). Therefore, the feature-relative flow was *rearward*, in contrast to the situation found in the gravity wave updrafts 4 and 5. The variation in propagation speed through the cell's life cycle helps explain the differences in spacing among the updraft features shown in Fig. 7.

The upward parcel accelerations (see Fig. 9a) occurred on the front-facing flanks of these updrafts despite the fact that the most buoyant air was concentrated on their rear-facing sides. The buoyancy (BUOY) and vertical perturbation pressure (VPGA) accelerations that combine to form PWDT are shown in Figs. 9b and 9c, respectively. BUOY and VPGA were in opposition nearly everywhere, but BUOY dominated VPGA on the front-facing flank of the growing cell ($x = 31$), while VPGA was the stronger on this updraft's rear-facing side ($x = 25$).

The front-facing side was also where the convectively unstable air was located. For feature 2, Figs. 9d and 9e show that while condensation was occurring through much of the updraft [QCLH, panel (e)], only on the updraft's front-facing side did the diabatic heating exceed the adiabatic cooling [TVPT, panel (d)]. The vertical θ_e gradient was negative (positive) on the updraft's front-facing (rear facing) sides (Fig. 9f). Upward motion resulted in net warming all along the upper surface (and cooling along the lower surface) of the high- θ_e ribbon. The same situation occurred in feature 3, the largely

dissipated cell $n - 1$, though the accelerations were weaker and encompassed less area.

Though the net warming was concentrated on the mature updraft's front-facing flank, the warmest air in the cell, associated with its original and least diluted parcels, was still in the process of moving toward the cell's rear-facing side at this time (section 2a). These original parcels carried their condensation warming along as they detrained from the updraft, and were replaced by more diluted (and therefore less convectively unstable) parcels (section 4c). Thus, condensation production and latent heating on the front-facing flank were smaller now than they were earlier in the cell's history. Intercomparison of Figs. 1b, 7a, and 1c shows the local potential temperature tendency ($\partial\theta'/\partial t$) was *negative* on that flank, which means the warming was being advected rearward faster than it was being generated. This is one hallmark of the weakening cell.

In the incipient new cell (feature 1), diabatic heating exceeded adiabatic cooling in the updraft everywhere above the LFC at $z \sim 1.6 \text{ km}$ (Fig. 9b). Above that level, PWDT was largely in phase with ascent (Fig. 9a) and in quadrature with advection (Fig. 8a), and was therefore intensifying the upper portion of the incipient cell's updraft without opposing its rearward motion. Part of the forced updraft's rear-facing side was experiencing net downward parcel accelerations at this time (above $x = 37$ in Fig. 9a). Although advection was carrying upward motion into this area (Fig. 8a), the LWDT (Fig. 8c) field shows that PWDT was dominant and thus the subsidence that caused the forced updraft to subsequently become isolated was in the process of being established there. This portion of the picture will be completed in section 4c below, which focuses specifically on the forced updraft's temporal variation.

b. Variation of the forced updraft as a manifestation of a convective feedback process

As noted earlier, the forced updraft's unsteadiness may be a fundamental reason why the storm itself is unsteady and multicellular. Below, the forced updraft's temporal variation is shown to be caused by the transient circulations established by the rearward-propagating convective cells. This is a convective feedback process, in which the cell acts to modulate the same lifting that helped established it, with an eventual negative influence on the cell itself.

Excluding mixing, the horizontal and vertical parcel acceleration equations are

$$\frac{du}{dt} = -\frac{1}{\bar{\rho}} \frac{\partial p'_d}{\partial x} - \frac{1}{\bar{\rho}} \frac{\partial p'_b}{\partial x} = F_{dx} + F_{bx} = F_{ix} \quad (3)$$

$$\frac{dw}{dt} = -\frac{1}{\bar{\rho}} \frac{\partial p'_d}{\partial z} - \left(\frac{1}{\bar{\rho}} \frac{\partial p'_b}{\partial z} - B' \right) = F_{dz} + F_{bz} = F_{iz}. \quad (4)$$

Perturbation pressure has been subdivided into its dy-

2D simulation - X-Z vertical velocity with tendency and equivalent potential temperature fields at 20460 sec

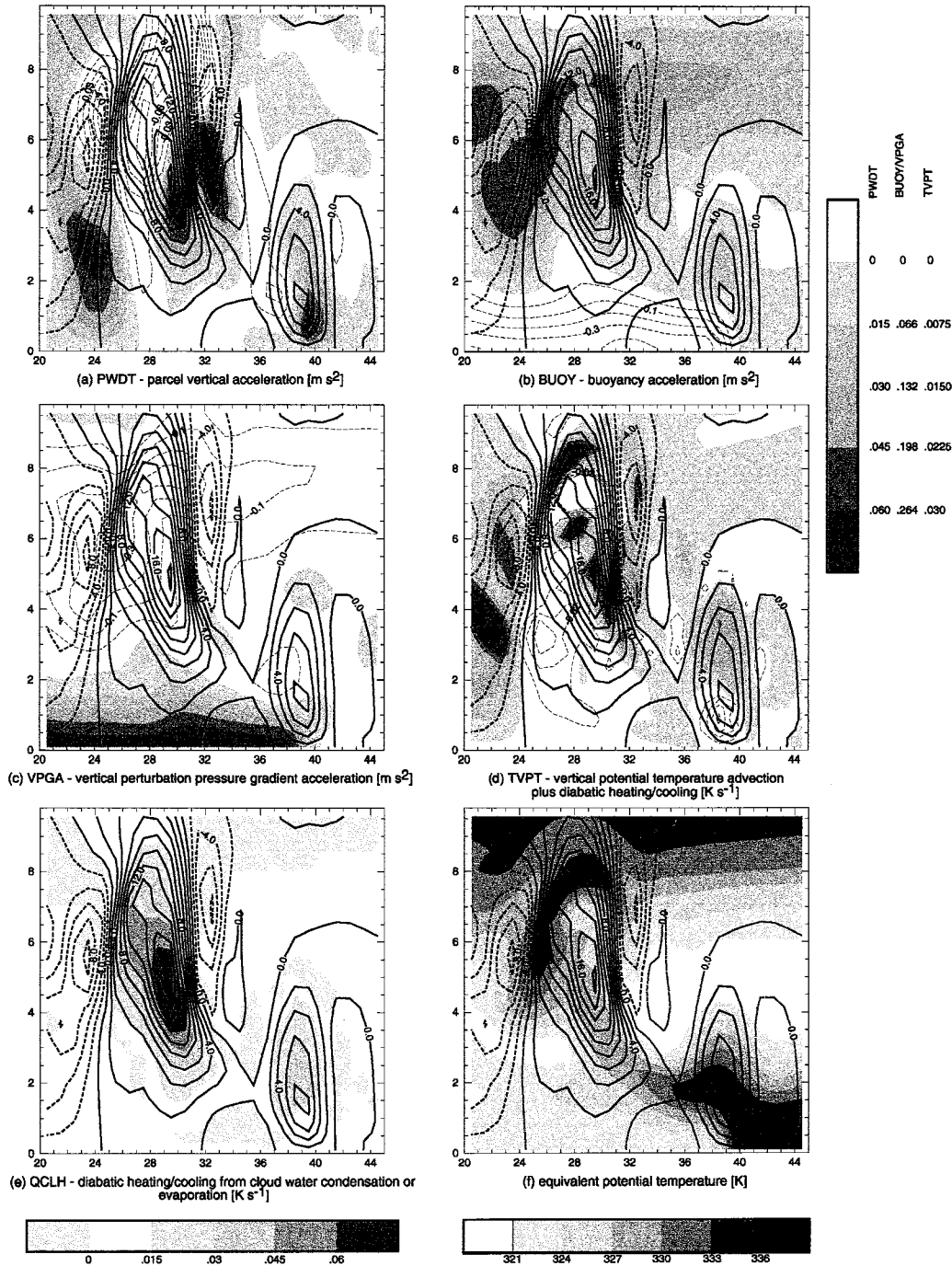


FIG. 9. Tendency and equivalent potential temperature fields shown with vertical velocity ($2 m s^{-1}$ contours) for a smaller subdomain than shown in Fig. 8, focusing on the incipient and matured cells (features 1 and 2). Panels are (a) PWDT, (b) BUOY, (c) VPQA, (d) TVPT, (e) QCLH, and (f) equivalent potential temperature. For acceleration fields, upward (downward) accelerations are shaded (contoured).

namic (p'_d) and buoyancy (p'_b) pressure components in the usual fashion (cf. Wilhelmson and Ogura 1972; Rotunno and Klemp 1982) and F stands generically for force per unit mass. By combining these equations, we can create vector acceleration fields defined as

$$\mathbf{F}_b = F_{bx}\mathbf{i} + F_{bz}\mathbf{k}$$

$$\mathbf{F}_d = F_{dx}\mathbf{i} + F_{dz}\mathbf{k}$$

$$\mathbf{F}_t = F_{tx}\mathbf{i} + F_{tz}\mathbf{k},$$

where \mathbf{F}_b , \mathbf{F}_d , and \mathbf{F}_t are, respectively, the buoyancy, dynamic, and total forcings (per unit mass); and \mathbf{i} and \mathbf{k} are the horizontal and vertical directional vectors. Note the vertical component of \mathbf{F}_t , F_{tz} , is PWDT. Chen (1991), Trier and Parsons (1995), and Trier et al. (1997), among others, have employed a similar decomposition of the vertical motion equation in isolation, wherein F_{bz} and F_{dz} were termed PZBY and PZDN, respectively.

First, we examine the buoyancy forcing field, \mathbf{F}_b . In the anelastic limit, buoyancy pressure is obtainable from the elliptic equation

$$\nabla^2 p'_b = \frac{\partial}{\partial z} \bar{\rho} B'. \quad (5)$$

Figure 10a sketches the buoyancy pressure gradient acceleration (BPGA) vector field, $-\bar{\rho}^{-1}\nabla p'_b$, associated with a rising, positively buoyant parcel of finite size.⁴ At the parcel's top, environmental air is being pushed out of the way, creating high perturbation buoyancy pressure. Meanwhile, the pressure is lowered at the parcel's bottom and thus the BPGA is directed downward within the parcel. It is also directed downward in the environment on either side of the parcel, where the compensating subsidence required by mass continuity is being induced.

Within a finite parcel, the downward-directed BPGA fails to restrain the buoyancy acceleration, and thus merely serves to slow the parcel's rate of rising (Houze 1993). When combined with B' , creating \mathbf{F}_b , the situation sketched in Fig. 10b is often obtained. A local circulation couplet is induced that tends to produce ascent within the parcel and subsidence on its flanks. The \mathbf{F}_b vector field traces the buoyancy-induced circulatory tendency.

Figure 10b can also be interpreted in the vorticity framework. Within the accuracy of the Boussinesq approximation, the 2D equation for the horizontal vorticity component normal to the x - z plane (η) is

$$\frac{d\eta}{dt} = -\frac{\partial B'}{\partial x}, \quad (6)$$

⁴ Houze (1993; see his Fig. 7.1) makes the useful analogy between the BPGA vector field associated with a buoyant element of finite size and the electric field enveloping a similarly finite region of electric charge.

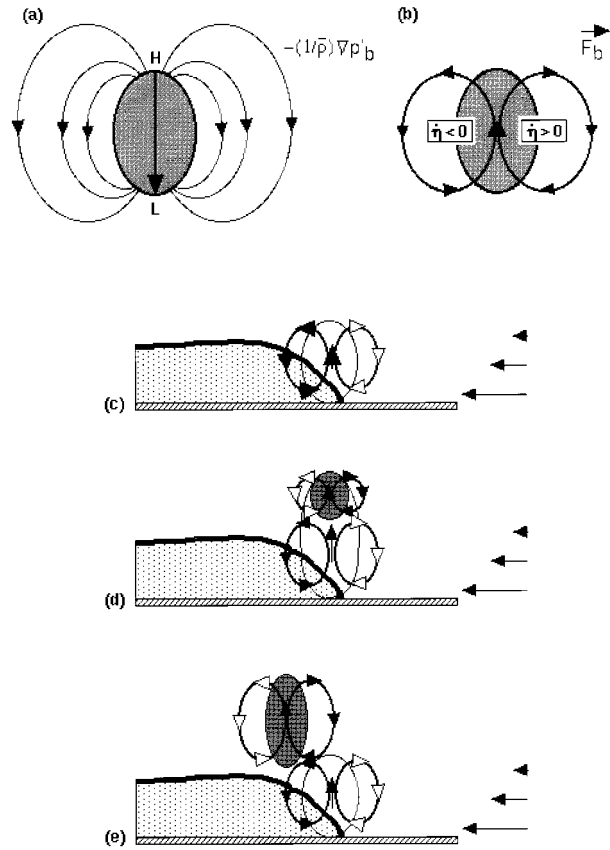


FIG. 10. Schematic illustrating the effect of an individual convective cell on the storm's low-level circulation (see text). Panel (a) shows the BPGA vector field associated with a finite, positively buoyant parcel, while (b) shows the full \mathbf{F}_b field and the circulatory tendency associated with baroclinic vorticity generation η . Panel (c) presents RKW's analysis of the circulation tendency at the subcloud cold pool (stippled region) boundary. Panel (d) adds a positively buoyant region with its attendant circulatory tendency, illustrating the initial formation of a convective cell. Panel (e) shows the cell's effect at a subsequent time.

which shows that parcels will acquire positive (negative) horizontal vorticity where horizontal buoyancy gradients are negative (positive). However, at the same level of approximation, (6) may be rewritten as

$$\frac{d\eta}{dt} = \mathbf{j} \cdot \nabla \times \mathbf{F}_b, \quad (7)$$

where \mathbf{j} is the y -directional vector. This shows the \mathbf{F}_b field vectors lie parallel to contours of $d\eta/dt$ (and $\partial B'/\partial x$) and thus outline the circulatory tendency associated with baroclinic vorticity generation. The equation reduces to this form because the curl of the dynamic forcing field, \mathbf{F}_d , is zero. Owing to the exclusion of dynamic forcing, the \mathbf{F}_b field is an incomplete representation of the total parcel acceleration. Still, it has the advantage of graphically demonstrating the instantaneous buoyancy-induced circulatory tendency.

Now we consider the low-level circulation at the

boundary of the negatively buoyant cold pool. Rotunno et al. (1988, hereafter RKW) used the vorticity framework to discuss its steady-state aspects. There are two opposing circulations, one baroclinically generated at the pool boundary (here, producing negative vorticity and a counterclockwise circulatory tendency), the other associated with the vertical wind shear (here, having positive horizontal vorticity and a clockwise circulation), that combine to establish the forced updraft (Fig. 10c). RKW argued that the relative strengths of these two circulations determine the path taken by parcels rising within the forced updraft. If equally matched, the parcels should continue rising vertically. When the cold pool's circulation is stronger, however, parcels will be impelled rearward as they rise. This "suboptimal" situation results in the characteristic FTR airflow of mature squall line circulations.

This steady-state analysis is now extended to incorporate the effects of buoyancy production associated with the intermittently produced, transient convective cells. At first, the positively buoyant air created by latent heating within the incipient cell is located *above the forced updraft*, as depicted in Fig. 10d. The warming induces a local circulation tendency that is superimposed upon the low-level circulation and thus affects the cold pool/shear circulatory balance. The new cell's circulation enhances the upward acceleration of parcels rising within the forced updraft while partially counteracting the rearward push due to the cold pool's circulation. As a result, the forced lifting is stronger and parcels follow a more vertically oriented path than they would have been able to without the condensationally generated heating. During this time, the forced lifting will strengthen and expand vertically.

The influence of the transient cell's circulation, however, depends on its phasing relative to the forced updraft. The dominance of the cold pool circulation ensures that the new cell and its positive buoyancy will soon be advected rearward. As it moves away from the forced updraft, the intensifying cell soon begins to exert a deleterious effect on the low-level lifting, as depicted in Fig. 10e. Instead of reinforcing upward accelerations in the forced lifting, the new cell is assisting the cold pool circulation in driving the rising parcels rearward. Thus, at this time, the forced lifting is weaker than it would have been in the absence of convection. As the cell continues moving rearward, however, its influence wanes, permitting the forced updraft to reintensify as the suppression disappears.

Figure 11 shows the buoyancy F_b and total parcel F , acceleration fields for the 2D simulation at the same times shown in Fig. 1. The buoyancy forcing field will be considered first. Note that the vectors depict instantaneous accelerations and not airflow.

At time A (Fig. 11a), the accelerations associated with the still-intensifying cell n located above $x = 32$ may be seen. The cell's most positively buoyant air resided within the updraft and its induced circulation served to

drive further ascent in the cell as well as downward motion on its flanks. The cold pool circulatory tendency can also be seen. At this time, the situation is as shown in Fig. 10e, with the cold pool and new cell circulatory tendencies combining to suppress the forced updraft, which was at its weakest strength recorded during the cell cycle (Fig. 2a).

A few minutes later, at time B (Fig. 11b), the established cell was stronger but also farther from the forced updraft, thus diminishing its impact on the low-level circulation. As this occurred, the forced updraft intensified rapidly and generated a shallow, localized region of condensational warming in the forced updraft just above the LFC, evidence that the generation of new cell $n + 1$ was under way. Initially, the newly established positive buoyancy helped strengthen the forced updraft beneath, as depicted in Fig. 10c. By time C (Fig. 11c), however, the new cell's induced circulation was already suppressing the forced updraft and, as a result, the low-level lifting weakened after this time (Fig. 2). The forced lifting strength continued to weaken until this cell also moved sufficiently far away, after time D (Fig. 11d).

Attention is now turned to the total forcing vector field F , incorporating the heretofore neglected dynamic pressure accelerations that can be inferred by comparing the two vector fields. Near the forced updraft, the total forcing field presents much the same picture as the buoyancy forcing did by itself. In the growing and mature cells, however, dynamic forcing augmented (opposed) the buoyancy circulation tendency on the updraft's lower (upper) portions, as previously shown (for the F_{dz} component) by Chen (1991). It appears that the dynamic effect became more significant as the cells aged and moved rearward.

Figure 11 suggests that both buoyancy and dynamic forcing play a role in generating the subsidence that appeared at $z \sim 2$ km on the forced updraft's rear-facing side and caused the growing cell to become cut off from the forced lifting. At time A (Fig. 11a), the buoyancy-forced circulatory tendency on the growing cell's front-facing side acted to push parcels there downward (see above $x = 37$). Though the dynamic forcing partially countered this descent in the middle troposphere, it augmented that occurring directly behind the forced updraft. Once the forced updraft began generating warming (time B; Fig. 11b), the incipient cell's buoyancy forcing took over the task of driving the subsidence there. Again, the dynamic forcing served to reinforce and intensify this descent. This accounts for the downward PWDT accelerations seen in a portion of the rear-facing side of the forced updraft just after time B (above $x = 37$ in Fig. 9a). Subsidence was being driven on the front-facing flank of the forced updraft as well around this time (above $x \sim 42$), with again both buoyancy and dynamic forcing contributing (Figs. 11b,c). The importance of this downdraft will be explored in sections 4c and 4d below.

In section 4a above, it was shown that while WADV

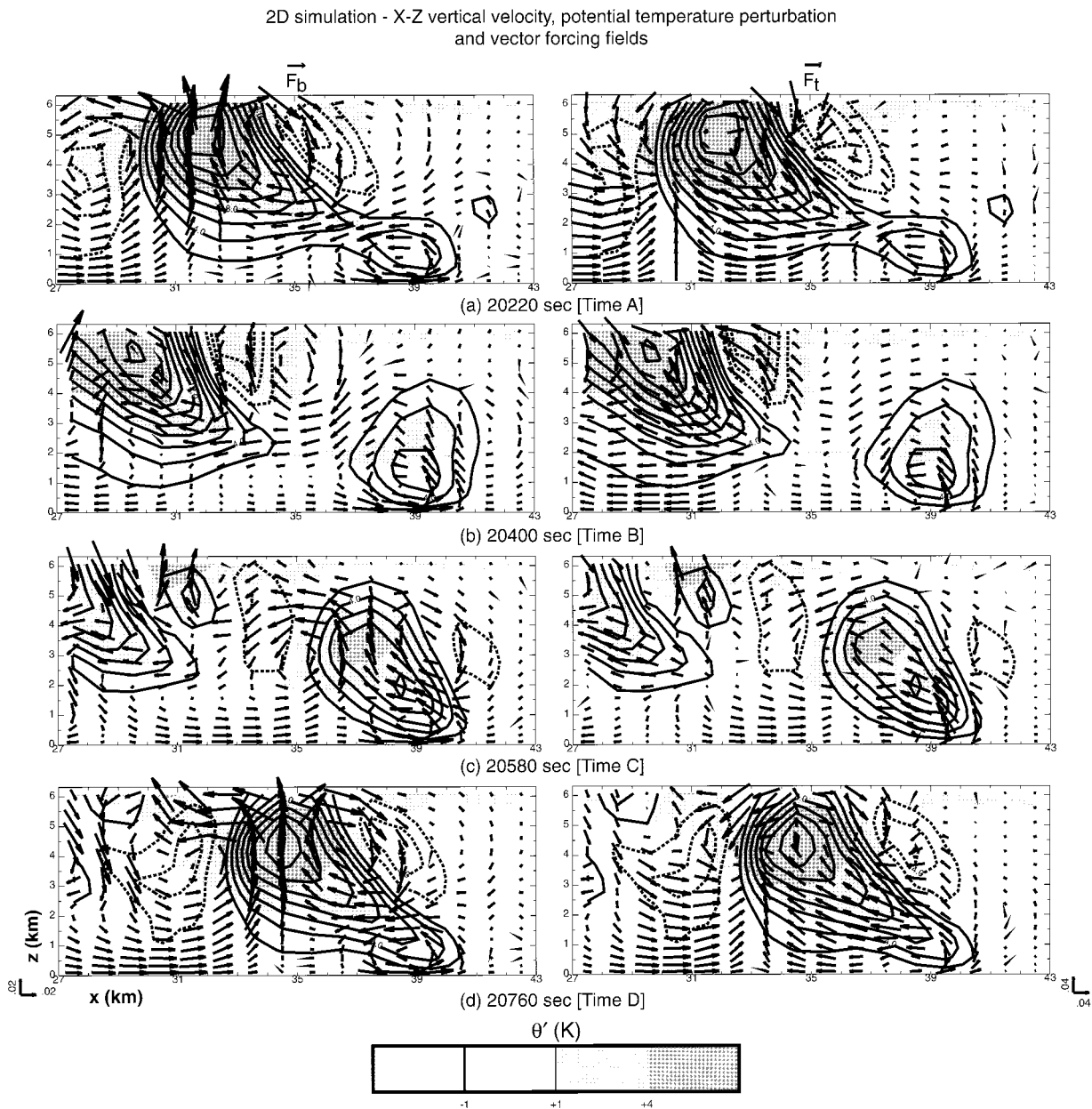


FIG. 11. Vector acceleration fields for the buoyancy (\mathbf{F}_b) and total (\mathbf{F}_t) forcings (per unit mass) for the 2D simulation, shown at the same four times presented in Fig. 1, with superposed vertical velocity (2 m s^{-1} contours) and potential temperature perturbation fields. Horizontal axes labeled relative to subdomain shown in Fig. 1.

and PWDT were in quadrature in the incipient cell between times B and C, they came into opposition as the cell matured. The \mathbf{F}_b and \mathbf{F}_t vector fields help show how that situation came about. (Again, the vertical component of \mathbf{F}_t is PWDT.) At time A, the warming and updraft were still largely collocated in the growing cell (above $x = 32$ in Fig. 11a). As the original, and most buoyant, air shifted to the cell's rear-facing flank (Figs. 1b and 3b), however, the buoyancy forcing stopped inducing upward accelerations within the rear-facing half of the cell, and indeed started opposing ascent there (compare

Fig. 11b). Dynamic accelerations enhanced this deleterious circulatory tendency near the updraft center (for $z \geq 4$). Thus, as the cell began detraining its original, most buoyant air, its rearward progress slowed even more due to the suppressing effect of that original air's buoyancy-induced circulatory tendency.

Figure 12 shows fields of \mathbf{F}_b and \mathbf{F}_t for selected vertical planes in the 3D simulation. The sequence of events is very similar to that seen in the 2D storm, especially within the temporally unsteady forced lifting zone. Panels 12a–c are x – z planes aligned along line B in Fig. 4,

3D simulation - vertical velocity, potential temperature perturbation and vector forcing fields

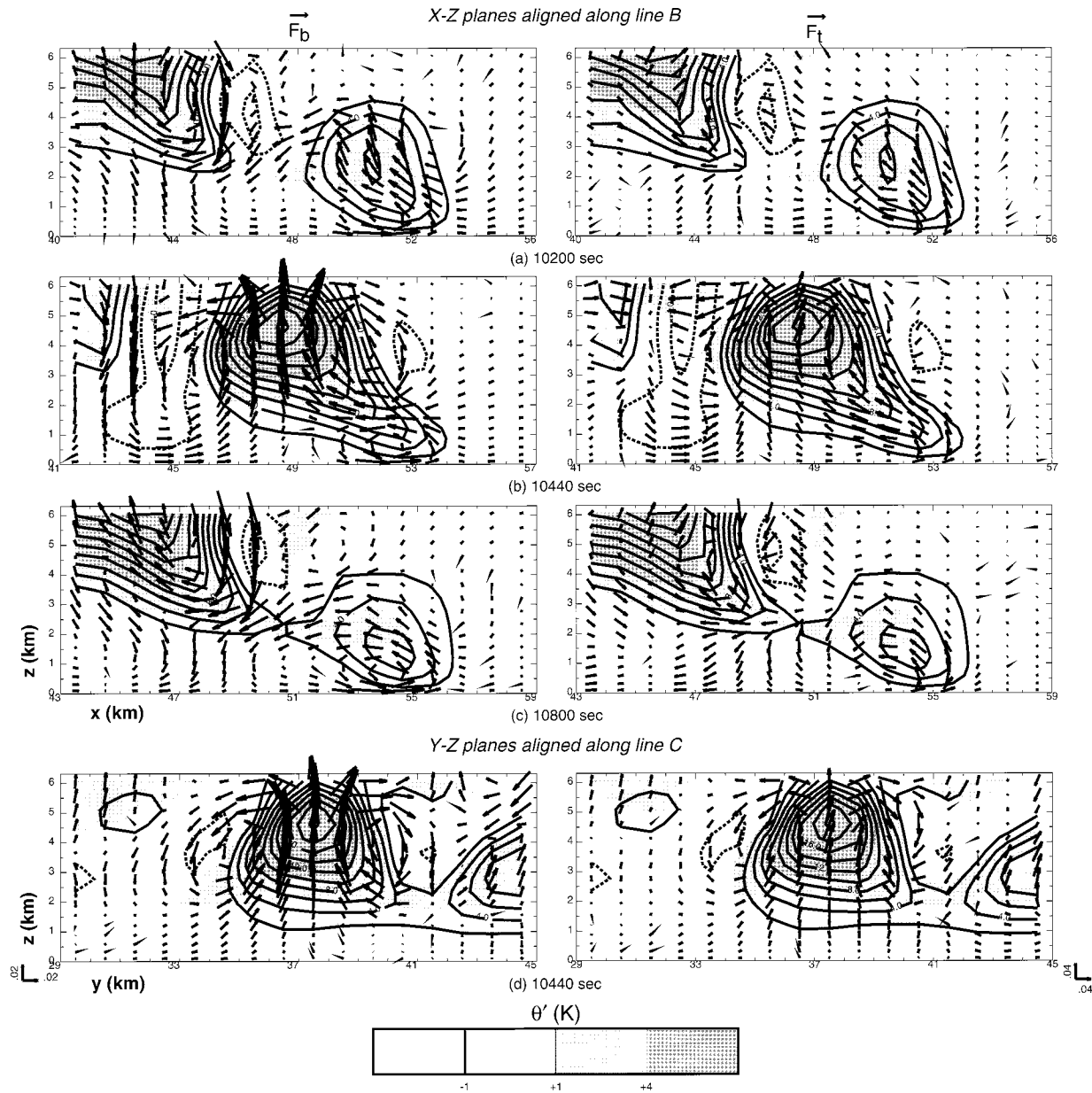


FIG. 12. As in Fig. 11 but for the 3D simulation, for the same four times presented in Fig. 4. The x - z and y - z cross sections were aligned along lines B and C shown in Fig. 4, respectively.

a location chosen simply because it passed through the strongest, most rapidly developing cell that was produced during the time period under examination. The slab symmetry of the 2D model, of course, presumes infinite extent in the alongline (y) direction. Figure 12d presents a y - z cross section oriented along Fig. 4b's line C, which passed through this cell's center during its rapid development period. The buoyant yet finite updrafts suppressed (induced) rising (sinking) motions in

their immediate surroundings. Indeed, because they were not infinite in the y direction, the 3D storm's updrafts were stronger, as it is appreciated that a given amount of buoyancy yields progressively larger vertical accelerations as the area of the parcel or updraft is narrowed (Houze 1993, 225).

Thus, the forced updraft's temporal variation appears to represent a *convective feedback process* in which the new convective cell first constructively and then de-

structively interferes with the forced updraft's strength. The cell's own circulation drives the subsidence that helps it become cut off from the forced updraft. The cell's suppression of the forced lifting temporarily reduces the influx of high- θ_e air from the low-level inflow after time C, at which time the previously mentioned isolated high- θ_e patch forms. The mixing that also must occur at this time is examined below.

c. Dilution of the high- θ_e inflow ribbon by episodic mixing induced by the cell's own circulation

In sections 3a and 3b, the growing new cell was shown to draw high- θ_e air upward from the low-level inflow, establishing a ribbon of such air within the FTR airflow that soon becomes diluted with lower- θ_e air. Figures 3 and 6 show there are two obvious sources for this air, from the cold pool and from midlevels ahead of the storm. To track the ribbon's dilution, the 2D simulation was restarted (at a time about 1 h before the time shown in Fig. 3a) with independent, quasi-conservative passive tracers placed into the two low- θ_e zones as well as into the high- θ_e inflow at low levels. A relatively small amount of tracer was placed in the cold pool in a shallow layer along the surface. Larger amounts of tracer were placed in the midlevel inflow ($\theta_e \leq 327$ K) and low-level inflow ($\theta_e \geq 333$ K).

Figure 13 presents the cold pool passive tracer fields at times A–D, while Fig. 14 shows the distributions of the other two tracers at time D, just after the isolated high- θ_e pocket formed. When the new cell was pushing upward at time C (Figs. 1c and 3c), it was free of contamination by either the cold pool (Fig. 13c) or midlevel inflow (not shown) low- θ_e tracers. The high- θ_e air patch became isolated shortly thereafter; note the low-level inflow tracer (Fig. 14a) closely mimicked this process. The distributions of the two low- θ_e tracers at this time (Figs. 13d and 14b) suggest that both participated in diluting the high- θ_e ribbon.

This is an *episodic* rather than continual mixing process, and appears to be the result of the growing cell's induced and transient circulation. Between times B and D, the rapidly growing new cell drove subsidence on its flanks (Figs. 3 and 11). The effect of the cell's front-facing subsidence shows in the θ_e field as a localized depression in the high- θ_e inflow layer's depth beneath the downdraft ($x = 39$ in Fig. 3d). This downward push of low- θ_e air appeared to assist its mixing into the high- θ_e ribbon at this time (Fig. 14b). Regarding the cold pool tracer, note that the updraft extended into the cold air, especially as the new cell starts moving rearward. Stable low- θ_e cold pool parcels there were forced to rise and were drawn into the high- θ_e ribbon in the cell's wake (Fig. 13d). Overall, the cell has taken on the appearance of an isolated, rising thermal with a toroidal circulation, and the mixing that occurred beneath it is consistent with the analyses presented by Turner (1964),

Bretherton and Smolarkiewicz (1989), and Johari (1992).

The remaining panels (Fig. 13) follow the transport of the cold pool tracer subsequent to the establishment of the new cell. At times A and B (Figs. 13a,b), the tracer became more thoroughly mixed through the intensifying mature cell. At time A, the updraft's highest- θ_e pocket was still well defined and undiluted, while at time B it was already contaminated by low- θ_e cold pool air. By time C, just before its identity was lost, the high- θ_e pocket became discontinuous; note that the pool tracer concentration was largest where the greatest dilution had occurred (indicated by the arrow).

Fovell and Ogura (1988) showed that in spite of the 2D geometry, low- θ_e air from the midlevel inflow could reach the cold pool owing to the storm's unsteadiness. This phenomenon was a critical component of Zipser's (1977) conceptual model. Figure 14b shows a large fraction of the intruding midlevel low- θ_e air was eventually deposited in the cold pool. Interestingly, the two low- θ_e tracers remained distinct in the areas they occupied at this time. In the cold pool and the high- θ_e ribbon, cold pool tracer concentration maxima coincided with distinct local minima in the midlevel tracer field (Figs. 13d, 14b).

Backward trajectories from the high- θ_e ribbon's dilution zone were also calculated (not shown); these served to confirm the interpretations drawn from the tracer distributions. Air parcels that had originated in the cold pool were especially easy to find. Fovell and Ogura (1989) showed w and θ_e fields (their Figs. 16 and 18) for a case in which forced lifting variation and episodic low- θ_e mixing also occurred. In that case, tracer and trajectory analyses suggested the midlevel inflow was the dominant source of low- θ_e air in the dilution zone. In the 3D model, of course, low- θ_e air from either source can also enter through the updraft's northern and southern flanks. The source of the stable air is probably less important than the fact that episodic dilution occurs and is associated with the cell's own induced circulation and rearward movement.

d. Timing of new cell establishment

New cell establishment usually does not occur until the suppressing effect of the previously established cell's circulation has waned. This can perhaps be described as an advective timescale, based upon the spatial extent of the cell and its attendant circulation and its speed and direction of movement relative to the storm's leading edge. As noted in the introduction, many studies have implicitly or explicitly concluded that a horizontal advective timescale operates in the multicellular storm.

In our view, this advective timescale is only the first phase of the cell generation process, necessary for the establishment of a new cell yet not sufficient to describe how quickly the next cell will form—if indeed it even does form. Once the suppression has been removed, the

2D simulation - X-Z fields of passive cold pool tracer

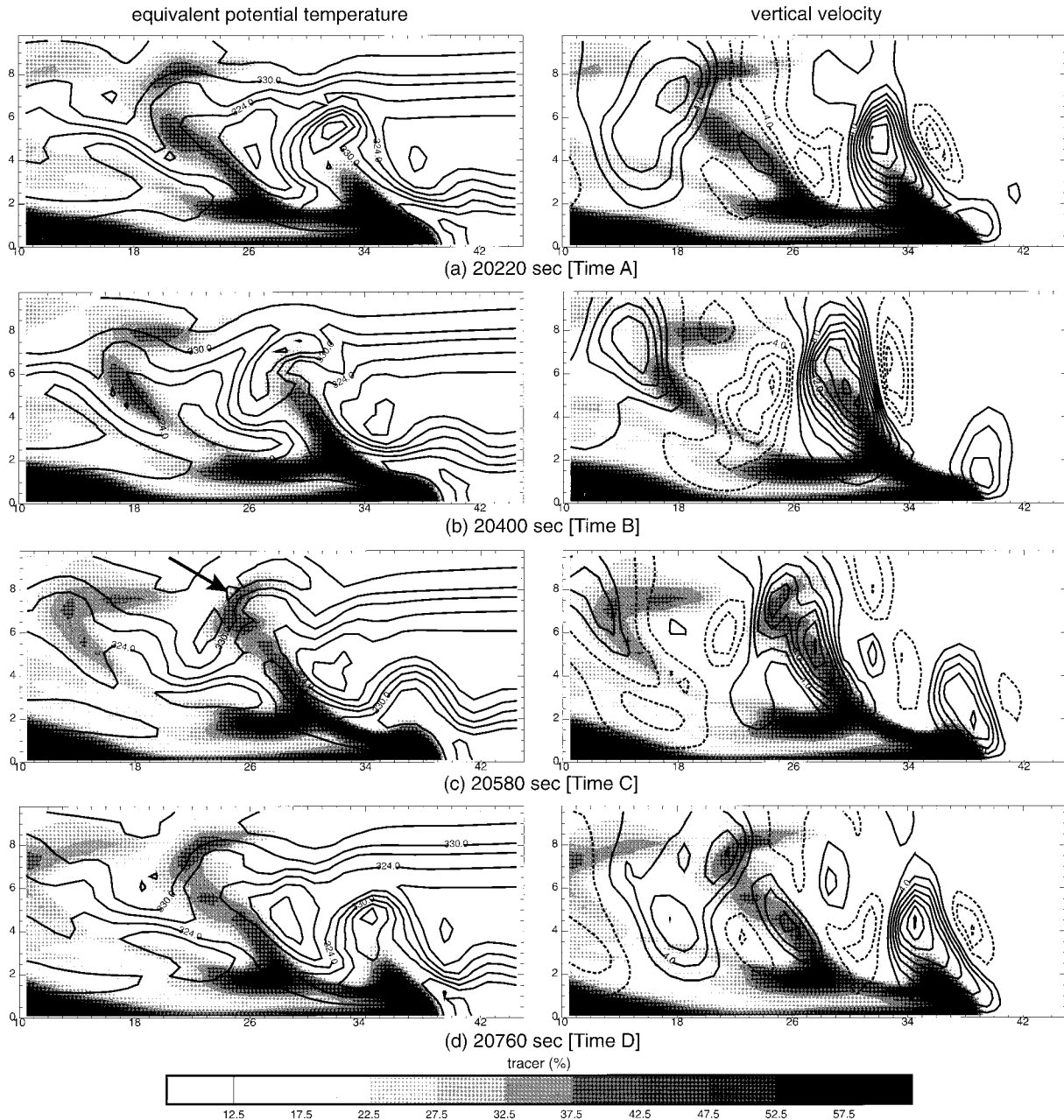


FIG. 13. Passive cold pool tracer fields (shaded) for the 2D simulation for the same four times shown in Fig. 1, with superposed equivalent potential temperature (3-K contours) and vertical velocity (2 m s^{-1} contours) fields. Shading density reflects relative tracer concentration; original concentration was 100% within the initialized area. Horizontal axes labeled relative to subdomain shown in Fig. 1.

forced lifting must be able to establish yet another new cell. This reestablishment represents the second phase of the process and appears to have its own timescale. Further, the reestablishment is by no means certain to occur. For example, if the storm's inflow environment changes, due to diurnal effects and/or the storm's propagation into a less convectively favorable region, new cell generation could cease. In those situations, the rees-

tablishment timescale is infinite and the storm's convective activity would terminate once mixing caused the previously generated cells to dissipate. Thus, in our view, the mature multicellular storm is always on the verge of extinction, which it avoids solely through the generation of replacement cells in some finite time.

Many factors can likely influence the reestablishment timescale, such as the storm inflow's CAPE, the strength

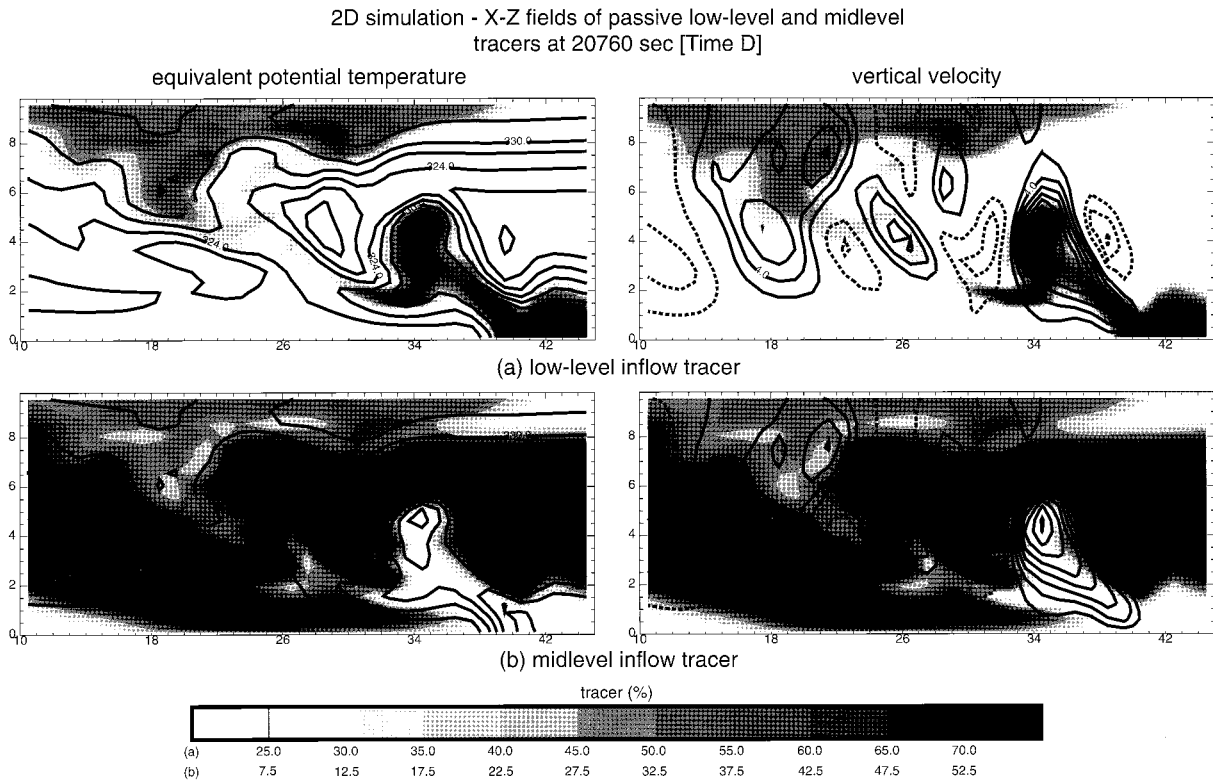


FIG. 14. As in Fig. 13 but for the (a) low-level inflow and (b) midlevel inflow passive tracers at 20760 s (identified as time D in text).

of the forced updraft at the time suppression ceases, and the LFC height. An especially favorable combination would probably permit the forced updraft to quickly regenerate a new cell. This is something we have not yet been able to systematically test because our analyses indicate the presence of another factor, or *convective trigger*, which itself constituted the reestablishment timescale. This trigger appeared as a transient, localized area in which the depth of the high- θ_e mixed layer ahead of the storm was deepened (Fig. 3). This phenomenon occurred in the 3D case as well (Fig. 6).

We now examine the formation and consequences of this convective trigger. At time B in the 2D case, the θ_e field (Fig. 3b) ahead of the storm ($x > 42$) was relatively horizontally homogeneous, although very small-amplitude horizontal undulations are detectable. As the new cell intensified, however, its circulation-induced front flank downdraft pushed midlevel low- θ_e air downward, compressing the high- θ_e mixed layer beneath it (time C; Fig. 3c). Just upstream, horizontal convergence caused a local deepening of the mixed layer (see arrow on Fig. 3c). This locally elevated mixed layer, a consequence of the growing cell's circulation, appeared to be important in the establishment of the next cell. A similar phenomenon occurred in the 3D simulation (Fig. 6), although the mixed layer was deepest just north of the plane shown.

Figure 15 shows perturbation water vapor fields from

the 2D case for times A–D as well as two additional times occurring in the period A–B. A layer of moistened air resided in the lower troposphere ahead of the storm; this resulted from the gentle lifting ($w < 1 \text{ m s}^{-1}$) of inflowing air parcels by the storm's buoyancy-induced *mesoscale* circulation and is a common feature of both 2D and 3D model storms (Fovell and Ogura 1988). Unsurprisingly, the local moistening maximum upstream of the forced lifting at time C (Fig. 15e) occurred where the high- θ_e mixed layer (Fig. 3c) was deepest (at $x = 44$). Both Figs. 3 and 15 show that after formation, the elevated layer approached the forced updraft. It was embedded in the storm inflow, and its progress was perhaps also aided by the upward and rearward movement of the growing cell and its flanking downdraft away from the forced updraft. At first, the air atop the elevated layer was unsaturated, but condensation occurred by time C (Fig. 15e), resulting in the formation of a shallow “daughter cloud”⁵ located a few kilometers ahead of the surface gust front.

A few minutes later (at times D and A; Figs. 15f and 15a), the daughter cloud's interior was positively buoyant and its circulation was slowly strengthening. Sub-

⁵ This term was apparently coined by Browning et al. (1976) to describe a similar phenomenon.

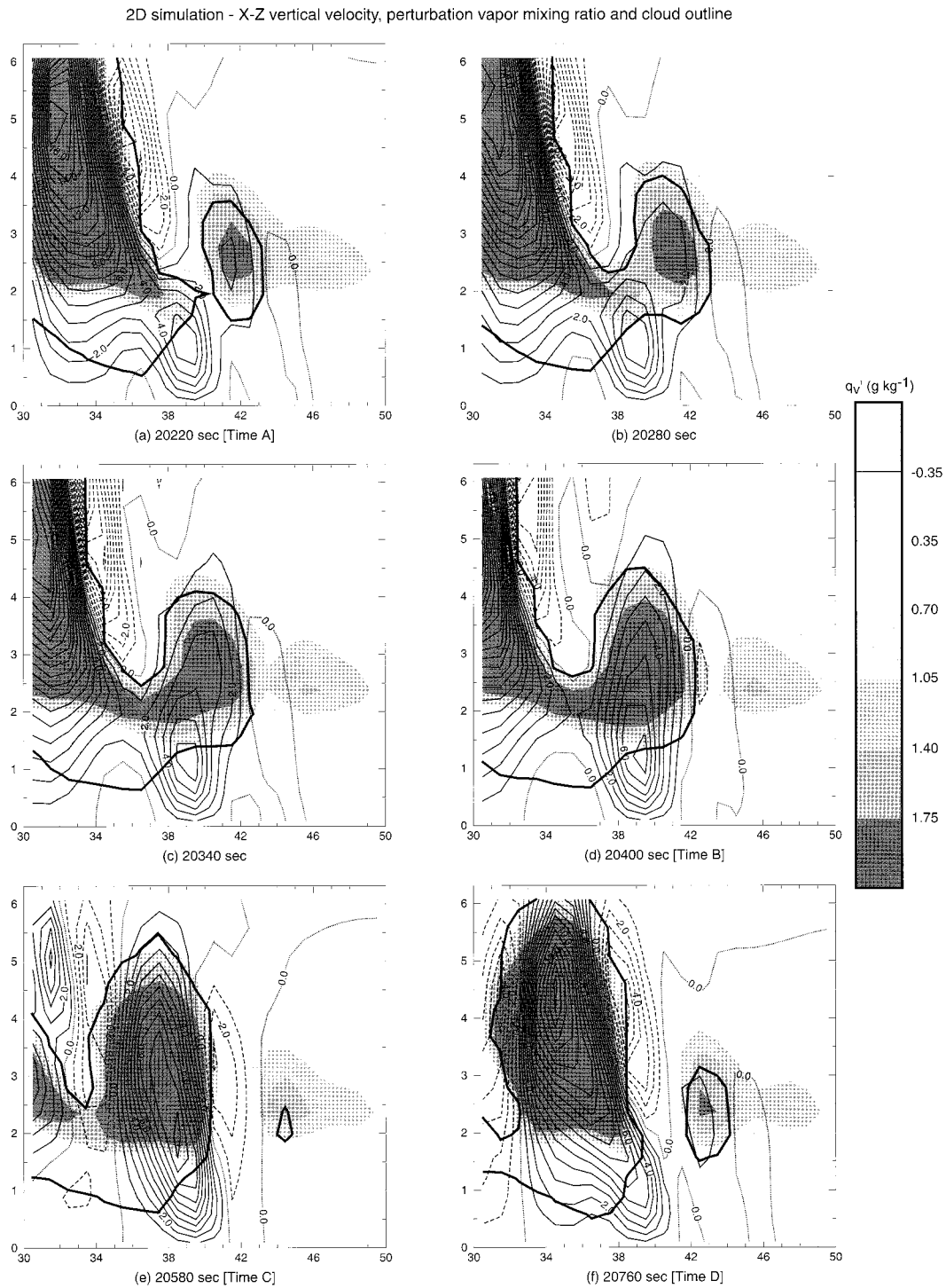


FIG. 15. Vertical velocity (1 m s^{-1} contours) and perturbation vapor mixing ratio fields from the 2D simulation for six times during the cell generation cycle examined in Fig. 1. Thick black curve is the cloud outline, represented by the 0.1 g kg^{-1} cloud water contour.

sidence appeared on its front-facing (east) side by time D (at $x = 46$). At this time, the forced updraft was also slowly strengthening (Fig. 2). It is quite possible that the forced lifting would eventually (and perhaps soon)

have accomplished sufficient lifting on its own to assure new cell generation. It is unclear in this case since the daughter cloud moved directly above the forced updraft (Figs. 15b,c) soon after time A. *The intensification of*

both features appeared to increase markedly after they came into phase. In the meantime, the subsidence on the daughter cloud's front-facing side had already contributed to elevating the high- θ_e mixed layer immediately upstream of it (at $x = 48$ and 47 in Figs. 15f and 15a, respectively). This eventually became the next daughter cloud, and triggered the next cell.

The elevated mixed layer/daughter cloud feature is termed a convective trigger because it appeared to hasten new cell generation. Though further work is required, it is suspected that the superposition of the slowly strengthening forced lifting and the weak, though intensifying, daughter cloud resulted in a more rapid reinvigoration of convection than would have occurred if either feature had been absent. While the details vary, a trigger of this nature has been commonly found in both 2D and 3D simulations employing this sounding as well as the (strongly similar) Weisman and Klemp (1982) environment. In this particular case, condensation within the elevated layer created a visual signature in the form of a daughter cloud; this also occurred in Fovell and Ogura's (1988) ice-free case (their Fig. 9). In FD's anelastic version of the 2D simulation, little condensation occurred prior to the elevated mixed layer's encounter with the forced lifting. Still, whether a cloud forms or not, the convective trigger represents a localized zone of deepened high- θ_e air that is especially favorable for the reinvigoration of convection.

Since the embedding flow swept the convective trigger toward the forced updraft, the second or reestablishment timescale in the cell generation process may be characterized by another advective timescale reflecting the trigger's width and the storm-relative flow speed, and perhaps also its initial location relative to the forced lifting. The relative flow speed is a function of the storm propagation speed, so faster storm movement should yield a shorter timescale. The trigger's horizontal scale should be proportional to that of the previous convective cell because it was established in response to that cell's induced circulation (which should also reflect the cell's spatial extent). Its initial location upstream of the forced updraft was determined by the width of the forward-side downdraft; as in Barnes et al. (1996), these downdrafts were found to be narrower than the cells that induced them. These scales can be influenced by numerical factors (see appendix) but the trigger appears to be a real, rather than numerically induced, phenomenon.

The two advective timescales are not easily separable because the convective trigger was generated in the environmental response to the previous cell's establishment and because the trigger moved toward the forced updraft concurrent with the previous cell's recession from it. However, intercomparison of a large number of simulations has suggested that the two timescales may be somewhat independent, if only because the cells and triggers are embedded in flows with different velocities and move at different speeds. Again, this requires fur-

ther work, and also evidence from observations needs to be acquired.

5. Synthesis and conclusions

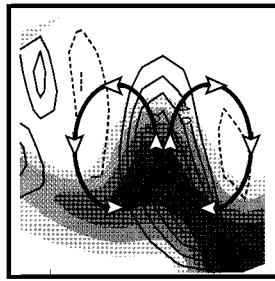
The analyses presented above are now integrated into a unified description of the life cycle of short-lived convective cells seen within mature, squall-type multicellular storms simulated by our cloud-resolving model. The cell life cycle from initiation to the commencement of dissipation is divided into three stages. Figure 16 represents a summary of these stages, presented in a reference frame centered on the convective cell updraft. Note that the reference frame moves with the updraft as it ages and propagates upward and rearward within the FTR airflow. The storm is propagating eastward relative to the ground.

The storm's dense subcloud cold pool represents an obstacle that pushes upwind against the low-level flow, establishing the gust front–forced updraft. According to RKW, the path taken by high- θ_e air parcels lifted in this updraft depends on the relative strengths of the opposing low-level circulations associated with the vertical wind shear and baroclinically generated vorticity at the gust front. In the typical mature squall line, the cold pool's circulation is dominant, and thus the parcels tend to continue their rearward storm-relative movement, establishing the storm's FTR airflow that is most clearly revealed in time-averaged fields.

The unsteady aspects of this circulation are now examined. In stage 1, the forcibly lifted air parcels encounter their LFC and become positively buoyant, marking the formation of a new convective cell. The newly created buoyancy induces a circulatory couplet that at this stage serves to strengthen upward motion within the new cell and the forced updraft beneath it as well as induce subsidence upon its flanks. As the updraft strengthens, it draws more high- θ_e air upward from the storm inflow, creating of a ribbon of potentially warm air that fuels the new cell's further development. Simultaneously, the flanking subsidence, in part reflecting the new cell's buoyancy-induced circulation, is having potentially important effects. On the rear-facing flank, the subsidence helps cut the new cell off from the previously generated cell. On the front-facing flank, it pushes low- θ_e air from midlevels downward, compressing the storm inflow's high- θ_e mixed layer below but elevating it farther upstream, the latter representing a phenomenon found to be influential in the establishment of the next convective development.

Like its predecessors, the growing cell updraft and its condensation warming are carried upward and rearward away from the forced lifting by the FTR airflow. During this time, the updraft and buoyancy perturbations are in phase, and so the cell's circulation intensifies its updraft without opposing its rearward translation. By stage 2, owing to this rearward movement, the cell's circulation has started to suppress the forced updraft;

Three stages in life cycle of a convective cell



Stage 1 (initiation of cell)

Buoyancy-induced circulation helps new cell rise, strengthen. Potentially warm air ingested from below.

Rise of cell establishes ribbon of potentially warm air in FTR airflow emanating from low-level storm inflow.



Stage 2 (maturation of cell)

Growing cell's buoyancy-induced circulation acts to weaken forced lifting, reduce potentially warm inflow.

Stable, potentially cold air mixes into cell's inflow from wake beneath, eroding its convective instability.

Cell's original, least diluted air concentrated near top of updraft. In 3D simulation, cell dynamically splits.



Stage 3 (dissipation of cell)

Cell's buoyancy-induced circulation on front-facing flank weakens as mixing erodes instability. Cell "splinters" and disorganizes.

During disorganization, original, least diluted air effectively "detrained" from splintered updraft, spreading about (above and to sides) of updraft shown. In consequence, on rear-facing side, buoyancy-induced circulation acts to dissipate rear-facing flank of updraft, slowing cell's rearward propagation.

FIG. 16. The three stages of a convective cell. Equivalent potential temperature (shaded) and vertical velocity (contoured) fields were taken from Fig. 3. Note the reference, frame shown is not fixed in space, but rather tracks the cell's principal updraft.

this continues until the new cell has moved sufficiently far out of the way. Until this happens, the influx of high- θ_e air into the FTR flow is reduced due to the weakened lifting.

As it moves away, the cell begins to draw air into it from below (its wake). This subsequent inflow differs in character from the cell's original air. It is a mixture of high- θ_e air from the low-level environment and low- θ_e air originating in the cold pool as well as the midlevel inflow on the storm's forward side. Stable cold pool air is drawn into the cell updraft as it is advected rearward, while the cell's forward-flank downdraft appears to help midlevel low- θ_e air mix into the high- θ_e ribbon. The cell's original, least diluted air resides near the top of the updraft at this time.

Thus, although the cell is still intensifying at this time, it is its own movement and induced circulation that are driving—or providing the opportunity for—the mixing

that is eroding the convective instability of its inflow. In these simulations, it appears that the cell dissipation inexorably occurs due to this dilution rather than the subsequent generation of a new convective cell on its upstream side. Thus, the cell has sown the seeds of its own demise.

This brings about stage 3, the period of cell dissipation and disorganization. The cell updraft resides along the slanted high- θ_e ribbon and, at least on its front-facing flank, the buoyancy-induced circulation still serves to maintain this updraft. However, owing to mixing, the circulatory strength there has decreased significantly. In the meantime, some of the cell's original, least diluted air has moved toward the rear-facing side, effectively being detrained from the updraft. In other words, the updraft moves rearward less rapidly than the air parcels within it. The circulation associated with this still positively buoyant air is acting to suppress vertical

motion on the cell's rear-facing side at this time. As a result, the cell's principal updraft is dissipating on its rear (west) side while regenerating on the opposite flank. During this stage, the cell's rearward translation is slowing even more as this buoyancy-induced circulation comes into opposition with rearward advection.

Stage 3 concludes when further mixing has completely eroded the convective instability in its neighborhood. The cell's remnants have degenerated into (or resulted in the excitation of) stable, rearward-propagating internal gravity waves that continue moving through the trailing region. As these waves move faster than the embedding flow, the end of stage 3 is also marked by a substantial increase in the storm-relative rearward movement of the remnant drafts, even though the FTR flow is weaker there than farther upstream. Yang and Houze (1995) also noted a similar speed increase (see their Fig. 16). This stage is not shown in Fig. 16 because the updrafts can no longer be considered convectively active.

Long before the cell has reached this point, the generation of the next new cell may already have commenced. From one point of view, new cell establishment can begin anytime after the previous development has ceased suppressing the forced lifting during stage 2. This appears to be interpretable as an advective timescale relating to the movement of the previous cell's circulation, incorporating its spatial extent and storm-relative recession speed. We have argued, however, that this represents only the first part of the cell generation timescale, one that provides a lower bound to the complete cell generation period. Once no longer suppressed, the forced lifting has to reestablish positive buoyancy above it, and this may require additional time even after the previous cell has moved sufficiently out of the way.

This reestablishment timescale may depend upon a variety of factors. Our simulations have suggested, however, that it may be shortened by the presence of a "convective trigger" in the low-level storm inflow. The previous cell's front-flank downdraft was shown to cause a local deepening of the high- θ_e inflow layer immediately upstream of it. In some model storms, such as those examined herein, the moist air atop this elevated layer achieves saturation, forming a "daughter cloud" that becomes positively buoyant and slowly intensifies while being advected toward the storm by the low-level inflow. Eventually, the daughter cloud passes directly over the now slowly intensifying forced updraft. As the cloud and forced updrafts come into phase, the cloud grows rapidly, resulting in the establishment of a vigorous, new convective cell. This portion of the cell generation cycle perhaps reflects another advective timescale, this one based on the spatial extent of the trigger and the speed of its embedding flow.

We have noted the presence of an episodically generated, elevated mixed layer in many of our 2D and 3D squall line simulations. In some cases, condensation does not form in the elevated layer, but new cell gen-

eration still appears to occur immediately after the elevated layer encounters the forced updraft. Thus, the daughter cloud merely provides a visual signature for the elevated layer in some cases. Again, the forced lifting could perhaps have generated a new cell on its own, in some finite time following the removal of the previous cell's suppression. The encounter with the elevated mixed layer merely accelerates the process, which is why it was termed a convective trigger.

Finally, we compare our interpretations with those of Yang and Houze (1995). On the basis of their simulations, YH concluded the "convective cells arise as gravity waves" formed in response to the forced updraft's continuous lifting, and interpreted the cutoff process as a gravity wave phenomenon. In our simulations, the convective cells do not degenerate into gravity waves until the conclusion of their life cycle, long after they were cut off from the forced updraft. However, there are several, potentially very significant, differences between YH's model storms and our own. Though both studies employed soundings taken during severe squall lines that occurred in the Oklahoma-Kansas area, their case's CAPE, being 33% larger than ours, is less typical of storms in this region and time of year (Bluestein and Jain 1985). In the 2D and 3D cases examined herein, the forced updraft is relatively weak and unsteady, and is also a shallow feature prior to the time of new cell establishment (see Figs. 1a and 5d). In contrast, in YH's 2D case, the forced lifting is steadier with twice the strength and depth of those seen herein⁶ (see their Fig. 14). Our new cells become established in the lower troposphere ($z \sim 2$ km) immediately above the shallow lifting. In contrast, YH's cells appear to "peel off" from the deep forced updraft, forming in the middle troposphere ($z \sim 6$ km, at their time 644 min) considerably farther downstream (~ 12 km) of the surface gust front. Our cells intensify rapidly and become strong; theirs are much weaker (their Fig. 14). Thus, our conclusions may differ because our storms' structures are dissimilar. We have been able to show that our cells are convectively active phenomena, and remain such for significant periods of time.

These conclusions apply specifically to multicellular squall lines possessing appreciably deep and intense cold pools and propagating into relatively quiescent environments. Therefore, the results may not be directly applicable to squall lines containing supercellular entities (e.g., Dudhia and Moncrieff 1989) or possessing different propagation mechanisms and/or inflow environments (Balaji and Clark 1988; Schmidt and Cotton 1990; Cram et al. 1992). In Balaji and Clark's (1988) multicellular storm, for instance, preexisting horizontal convective rolls in the inflow environment provided the

⁶ Insufficient information is given for their 3D case.

2D simulation - X-Z vertical velocity, perturbation vapor mixing ratio and cloud outline
for 1 km resolution and four computational dissipation rates (DR)

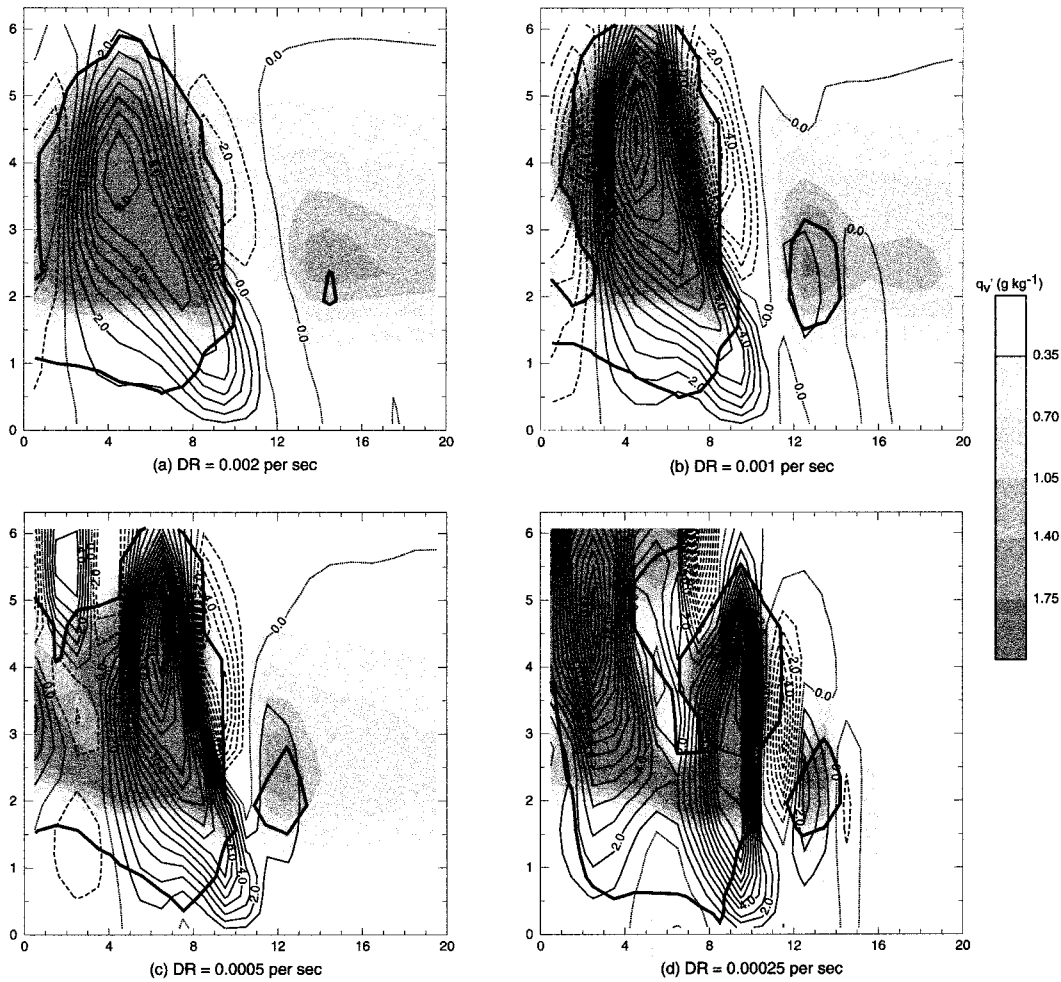


FIG. A1. Vertical velocity (1 m s^{-1} contours) and perturbation vapor mixing ratio fields for four 2D simulations employing different horizontal computational dissipation rates (DR; s^{-1}), for comparison with Fig. 15. Thick black curve is the cloud outline, represented by the 0.1 g kg^{-1} cloud water contour. For clarity, negative vapor mixing ratio regions are not shown. Panel (b) is the same as Fig. 15f. Horizontal axis labels are relative to subdomains depicted. Approximately the same relative time within each case's cell generation cycle is shown.

triggering mechanism for new cells. Such rolls were not present in the simulations presented herein.

Convective initiation and the convective cell life cycle are important phenomena that are receiving an increasing amount of attention. With the advent of more sensitive modern radars, it may soon be possible to observe details relating to these phenomena as well as to better distinguish among different multicellular storm structures. This would be necessary to adequately validate the discussion and conclusions presented herein.

Acknowledgments. This work was supported by the National Science Foundation (NSF) under Grant ATM94-21847. The ARPS model was developed at the Center for Analysis and Prediction of Storms (CAPS) at the University of Oklahoma. CAPS is supported by

the NSF and the Federal Aviation Administration through combined Grant ATM92-20009.

APPENDIX

Sensitivity of the Results to Horizontal Computational Mixing

The subcloud cold pool boundary is a cold front. In the absence of fluid diffusion (mixing) and Coriolis accelerations, the frontal boundary zone will contract to infinitesimal width (Emanuel 1985). In the numerical model, spatial resolution limits the contraction, and the parameterized subgrid-scale turbulence provides part of the mixing. However, Droegemeier and Wilhelmson (1987) pointed out that *computational* mixing also op-

poses the frontal collapse. Fovell (1996) noted that, at least in the 2D model, the cold pool air's substantial stability restrained the generation of turbulence in the frontal zone, leaving computational mixing and resolution as the primary determinants of the frontal zone width. This width directly influenced the horizontal scales of the forced updraft, which in turn determined the widths of the convective cells and related features such as the daughter clouds (convective triggers).

Herein, the sensitivity to the horizontal computational mixing is demonstrated and assessed. This mixing may be expressed as a dissipation rate (s^{-1}). For fixed horizontal resolution (1 km) in both model geometries, dissipation rates from 2×10^{-3} to $2.5 \times 10^{-4} s^{-1}$ were examined. Results from the 2D model are presented in Fig. A1, provided for comparison with Fig. 15. Decreasing the computational mixing resulted in substantial horizontal scale contraction, which was accompanied by a shortening of the cell generation period.⁷ The storms were still multicellular, and their cell life cycles strongly resembled that investigated in section 4, despite the varying horizontal and temporal scales. This dynamical similarity supports the interpretations and conclusions presented in this report.

The cell updrafts and their induced circulations intensified as they narrowed, as did the convective triggers. The trigger appears to be the smallest-scale important feature within the storm. Sensitivity to the domain translation speed increased dramatically as the numerical (grid point) widths of these features contracted. The least computationally diffusive run (Fig. A1d), in which both the cells and the trigger were poorly resolved, was *extremely sensitive* to the domain speed as well as the order of the horizontal advection scheme. Advection schemes typically handle shorter numerical wavelengths more poorly than longer ones, and differ most in their handling of these waves. Especially in this case, changing the domain speed affected the timing of new cell development, perhaps because it affected the speed at which the trigger approached the forced lifting (through advection error) and thus its degree of development prior to arriving there. This can also affect the mode of temporal behavior, which FD examined in detail. As noted in section 2, we chose to present simulations that are comparatively insensitive to the chosen Galilean transformation and thus relatively free of advection error.

The 3D cases (not shown) appeared to be relatively less sensitive to alterations of this artificial mixing, per-

haps because they tended to generate greater amounts of turbulence in their frontal zones. Weisman et al. (1997) have also discussed the effects of computational smoothing on their model storms. Extensive testing has also suggested that the development of these elevated mixed layers are not model artifacts, even in cases in which they are poorly resolved. This was ascertained by using different advection schemes and even different models.

REFERENCES

- Balaji, V., and T. L. Clark, 1988: Scale selection in locally forced convective fields and the initiation of deep cumulus. *J. Atmos. Sci.*, **45**, 3188–3211.
- Barnes, G. M., J. C. Fankhauser, and W. D. Browning, 1996: Evolution of the vertical mass flux and diagnosed net lateral mixing in isolated convective clouds. *Mon. Wea. Rev.*, **124**, 2764–2784.
- Bluestein, H. B., and M. H. Jain, 1985: Formation of mesoscale lines of precipitation: Severe squall lines in Oklahoma during spring. *J. Atmos. Sci.*, **42**, 1711–1732.
- Blyth, A. M., W. A. Cooper, and J. B. Jensen, 1988: A study of the source of entrained air in Montana cumuli. *J. Atmos. Sci.*, **45**, 3944–3964.
- Bretherton, C. S., and P. K. Smolarkiewicz, 1989: Gravity waves, compensating subsidence and detrainment around cumulus clouds. *J. Atmos. Sci.*, **46**, 740–759.
- Browning, K. A., J. C. Fankhauser, J.-P. Chalon, P. J. Eccles, R. C. Strauch, F. H. Merrem, D. J. Musil, E. L. May, and W. R. Sand, 1976: Structure of an evolving hailstorm. Part V: Synthesis and implications for hail growth and hail suppression. *Mon. Wea. Rev.*, **104**, 603–610.
- Chen, C.-S., 1991: A numerical study of a squall line over the Taiwan Strait during TAMEX IOP 2. *Mon. Wea. Rev.*, **119**, 2677–2698.
- Cram, J. M., R. A. Pielke, and W. R. Cotton, 1992: Numerical simulation and analysis of a prefrontal squall line. Part II: Propagation of the squall line as an internal gravity wave. *J. Atmos. Sci.*, **49**, 209–225.
- Droegemeier, K. K., and R. B. Wilhelmson, 1987: Numerical simulation of thunderstorm outflow dynamics. Part I: Outflow sensitivity experiments and turbulence dynamics. *J. Atmos. Sci.*, **44**, 1180–1210.
- Dudhia, J., and M. W. Moncrieff, 1989: A three-dimensional numerical study of an Oklahoma squall line containing right-flank supercells. *J. Atmos. Sci.*, **46**, 3363–3391.
- , —, and D. W. K. So, 1987: The two-dimensional dynamics of West African squall lines. *Quart. J. Roy. Meteor. Soc.*, **113**, 121–146.
- Emanuel, K. A., 1985: What limits front formation? *Nature*, **315**, 99.
- , 1994: *Atmospheric Convection*. Oxford University Press, 580 pp.
- Fovell, R. G., 1991: Influence of the Coriolis force on two-dimensional model storms. *Mon. Wea. Rev.*, **119**, 606–630.
- , 1996: Horizontal scale selection of convective cells in numerically simulated squall lines. Preprints, *Seventh Conf. on Mesoscale Processes*, Reading, United Kingdom, Amer. Meteor. Soc., 471–472.
- , and Y. Ogura, 1988: Numerical simulation of a midlatitude squall line in two dimensions. *J. Atmos. Sci.*, **45**, 3846–3879.
- , and —, 1989: Effect of vertical wind shear on numerically simulated multicell storm structure. *J. Atmos. Sci.*, **46**, 3144–3176.
- , and P. S. Dailey, 1995: The temporal behavior of numerically simulated multicell-type storms. Part I: Modes of behavior. *J. Atmos. Sci.*, **52**, 2073–2095.
- Hane, C. E., C. J. Kessinger, and P. S. Ray, 1987: The Oklahoma squall line of 19 May 1977. Part II: Mechanisms for maintenance

⁷ Storm speeds for the four cases were 14.9, 15.3, 15.9, and 14.5 $m s^{-1}$. Fundamental cell regeneration periods were 13.5, 11.0, 8.0, and 7.0 min, respectively. The case with the $0.00025 s^{-1}$ dissipation rate was aperiodic and suffered from weakly amplifying nonlinear instability, especially in the upper troposphere (above the subdomain depicted). Slightly smaller dissipation resulted in rapidly growing instability. The other cases were judged simply periodic.

- of the region of strong convection. *J. Atmos. Sci.*, **44**, 2866–2883.
- Houze, R. A., Jr., 1993: *Cloud Dynamics*. Academic Press, 573 pp.
- Johari, H., 1992: Mixing in thermals with and without buoyancy reversal. *J. Atmos. Sci.*, **49**, 1412–1426.
- Kessler, E., 1969: *On the Distribution and Continuity of Water Substance in Atmospheric Circulation*. *Meteor. Monogr.*, No. 32, Amer. Meteor. Soc., 84 pp.
- Klemp, J. B., 1987: Dynamics of tornadic thunderstorms. *Annu. Rev. Fluid Mech.*, **19**, 369–402.
- , and R. B. Wilhelmson, 1978: The simulation of three-dimensional convective storm dynamics. *J. Atmos. Sci.*, **35**, 1070–1096.
- Miller, M. J., 1978: The Hampstead storm: A numerical simulation of a quasi-steady cumulonimbus system. *Quart. J. Roy. Meteor. Soc.*, **104**, 413–427.
- Ogura, Y., and M.-T. Liou, 1980: The structure of a midlatitude squall line: A case study. *J. Atmos. Sci.*, **37**, 553–567.
- Rotunno, R., and J. B. Klemp, 1982: The influence of shear-induced pressure gradient on thunderstorm motion. *Mon. Wea. Rev.*, **110**, 136–151.
- , —, and M. L. Weisman, 1988: A theory for strong, long lived squall lines. *J. Atmos. Sci.*, **45**, 463–485.
- Schmidt, J. M., and W. R. Cotton, 1990: Interactions between upper and lower tropospheric gravity waves on squall line structure and maintenance. *J. Atmos. Sci.*, **47**, 1205–1222.
- Smull, B. F., and R. A. Houze, Jr., 1985: A midlatitude squall line with a trailing region of stratiform rain: Radar and satellite observations. *Mon. Wea. Rev.*, **113**, 117–133.
- Thorpe, A. J., M. J. Miller, and M. W. Moncrieff, 1982: Two-dimensional convection in non-constant shear: A model of midlatitude squall lines. *Quart. J. Roy. Meteor. Soc.*, **108**, 739–762.
- Trier, S. B., and D. B. Parsons, 1995: Updraft dynamics within a numerically simulated subtropical rainband. *Mon. Wea. Rev.*, **123**, 39–58.
- , W. C. Skamarock, and M. A. LeMone, 1997: Structure and evolution of the 22 February 1993 TOGA COARE squall line: Organization mechanisms inferred from numerical simulation. *J. Atmos. Sci.*, **54**, 386–407.
- Turner, J. S., 1964: The flow into an expanding spherical vortex. *J. Fluid. Mech.*, **18**, 195–208.
- Weisman, M. L., and J. B. Klemp, 1982: The dependence of numerically simulated convective storms on vertical wind shear and buoyancy. *Mon. Wea. Rev.*, **110**, 504–520.
- , W. C. Skamarock, and J. B. Klemp, 1997: The resolution dependence of explicitly modeled convective systems. *Mon. Wea. Rev.*, **125**, 527–548.
- Wilhelmson, R. B., and Y. Ogura, 1972: The pressure perturbation and the numerical modeling of a cloud. *J. Atmos. Sci.*, **29**, 1295–1307.
- , and C.-S. Chen, 1982: A simulation of the development of successive cells along a cold outflow boundary. *J. Atmos. Sci.*, **39**, 1466–1483.
- Xue, M., K. K. Droegemeier, V. Wong, A. Shapiro, and K. Brewster, 1995: ARPS Version 4.0 user's guide. Center for Analysis and Prediction of Storms, Univ. of Oklahoma, 380 pp. [Available from CAPS, 100 E. Boyd St., Norman, OK 73019.]
- Yang, M.-J., and R. A. Houze, Jr., 1995: Multicell squall-line structure as a manifestation of vertically trapped gravity waves. *Mon. Wea. Rev.*, **123**, 641–660.
- Zipser, E. J., 1977: Mesoscale and convective-scale downdrafts as distinct components of squall-line structure. *Mon. Wea. Rev.*, **105**, 1568–1589.